Supporting Information

Synthesis and comparison of iso-structural *f*-block metal complexes (Ce, U, Np, Pu) featuring η^6-arene interactions

Jesse Murillo,[a,b] *Conrad A. P. Goodwin,*[b] *Lauren Stevens,*[b,c] *Skye Fortier*[*,a] *Andrew J. Gaunt,*[*,b] *and Brian L. Scott*[c]

[a] Department of Chemistry and Biochemistry, University of Texas at El Paso, El Paso, Texas 79968, USA

[b] Chemistry Division, Los Alamos National Laboratory, Los Alamos, New Mexico, 87545 USA

[c] Materials Physics and Applications Division, Los Alamos National Laboratory, Los Alamos, New Mexico 87545, USA

*Corresponding Authors: Andrew J. Gaunt (E-mail: gaunt@lanl.gov) and S. Fortier (E-mail: asfortier@utep.edu)

Table of Contents

Materials and Methods

Caution! ^{237}Np decays principally through α-emission (Q_α = 4.958 MeV) ($t_{1/2}$ = 2.144(7) × 10^6 years) with a relatively high specific-activity (a = 26.04 MBq g^{-1}) in comparison to ^{238}U and ^{232}Th requiring analyses of hazards and implementation of additional safety controls. ^{237}Np establishes a secular equilibrium with the potent β-emitter ^{233}Pa ($t_{1/2}$ = 26.975(13) days, a = 777 TBq g^{-1}) and associated γ-ray emission (most significant γ-branching ratio for ^{233}Pa is 39% for the 312 keV line). ^{239}Pu decays principally through α-emission (Q_α = 5.244 MeV) ($t_{1/2}$ = 24,110(30) years) with β/γ -emission hazards also posed by daughter products and other isotopes present in nominally weapons-grade plutonium. Hence, all studies that involved manipulation of ^{237}Np or ^{239}Pu material were conducted in a specialized transuranium radiological designated area equipped with high efficiency particulate in air (HEPA) filtered hoods and in negative pressure gloveboxes. Safety controls included continuous air monitoring for airborne α-emitting particles and use of hand-held radiation monitoring equipment. Entrance to the laboratory space was controlled with a hand and foot radiation monitoring instrument and a full body personal contamination monitoring station. The handling of free-flowing solids was restricted to be within negative pressure gloveboxes equipped with HEPA filters. In addition to standard laboratory PPE, aqueous solutions were handled using multiple layers of gloves (of a material compatible with the chemicals being handled) combined with DuPont™ Tyvek® 400 sleeves to provide overlapping coverage of the arms.

All air and moisture-sensitive operations regarding ligand, uranium, and cerium complexation, were performed in a MBraun dry box under an atmosphere of ultra-high purity dinitrogen or argon. For transuranium reactions conducted at Los Alamos National Laboratory, syntheses were carried

out in a negative pressure, transuranium capable, MBraun LabMaster glovebox. The atmosphere was maintained with a standalone Vacuum Atmosphere GenesisTM oxygen and moisture removal system, and atmosphere suitability was verified using a dilute toluene solution of $[Ti(Cp)_2(\mu\text{-}Cl)]_2$. Solvents used in the synthesis of non-transuranium compounds were dried using a Pure Process Technology Solvent Purification System and subsequently stored under a dinitrogen atmosphere over activated 4 Å molecular sieves. For transuranium compounds reported, solvents used were purchased anhydrous and stored for several weeks over activated 4 Å molecular sieves before use. The $CeCl_3$ and CeI_3 were purchased from Strem Chemicals Inc. in anhydrous form at 99.9% purity. $UCl_3(THF)_2$ and $UI_3(THF)_4$ were synthesized using previously reported methods.[1, 2] $^{237}NpO_2$ powder, obtained commercially from the National Isotope Development Center (managed by the U.S. Department of Energy Isotope Program), was dissolved in nitric acid, precipitated as a hydroxide, redissolved in hydrochloric acid, redox conditioned with hydroxylamine hydrochloride to Np(IV) then purified on an anion exchange column to result in an elute fraction of an oxidation state pure Np(IV) stock solution in multi-molar aqueous HCl (the Np(IV) was eluted from the column with 0.5 M HCl into a collection vial containing concentrated HCl). An aliquot of the Np(IV) stock solution was blown to dryness under flow of UHP argon gas and subsequently used to prepare the anhydrous $NpCl_4(DME)_2$ followed by $NpI_3(THF)_4$ as previously described.[3] For ^{239}Pu, an in-house (LANL) stock solution of Pu(IV) in multi-molar HCl was used to prepare the anhydrous $PuCl_4(DME)_2$ followed by $PuI_3(THF)_4$ as previously described.[3] *Some syntheses reported herein employ an in-situ method for generating the trivalent actinide starting materials. Those syntheses were performed prior to the development of the more reliable and optimized routes to* $NpI_3(THF)_4$ and $PuI_3(THF)_4$ *reported in the intervening period of time.*[3] Benzene-d_6 and THF-d_8 were purchased from Cambridge Isotope Laboratories Inc. and dried over

activated 4 Å molecular sieves for 24 h prior to use. Celite used for filtration was dried under vacuum while heating at 250 °C for 24 h, subsequently cooled under vacuum, and stored under dinitrogen. Alternatively, reactions were filtered by glass filter disk which was dried in vacuum oven for at least 24 h prior to use. $[(K(DME)_2)_2L^{Ar}]$ and $L^{Ar}U(I)(DME)$ were synthesized according to literature procedure.[4]

NMR spectral data reported for all uranium and cerium complexes were measured using a Bruker AVANCE III 400 MHz spectrometer. For all neptunium and plutonium complexes, NMR spectra were recorded on a Bruker AVANCE II 400 MHz spectrometer. The ^{1}H NMR spectra are referenced to $SiMe_4$ using the residual ^{1}H solvent peaks as internal standards. UV-vis/NIR spectra for uranium and cerium complexes were recorded on a Varian Cary 5000 spectrophotometer using THF as a solvent. All neptunium and plutonium UV-vis/NIR spectra were recorded on a Varian Cary 6000i UV-vis/NIR spectrophotometer using toluene as a solvent. All UV-vis/NIR measurements were made in a 1 cm path length screw-capped quartz cuvette. Where ε values are reported for molecular complexes, there is an inherent error due to the small quantities of weighed material, as is typical for similar chemistry performed on similar scales and working conditions. Therefore, the ε values should not be used in a rigorous quantitative analytical sense. However, the ε values reported are still useful qualitative metrics that we determine based on weight of crystal dissolved and solvent weight within the error of our balance instrumentation. All spectroscopic data were taken at room temperature. Elemental analyses (EA) were performed by Midwest Microlabs, LLC. For all samples sent for EA, samples were sent as crystalline solids from batches from were positively identified by single-crystal X-ray diffraction.

For compounds $\mathbf{1}^{Np}$, $\mathbf{2}^{Np}$, $\mathbf{2}^{Ce}$, $\mathbf{3}^{Np}$, $\mathbf{3}^{U}$, $\mathbf{3}^{Ce}$ and $\mathbf{3}^{Pu}$, cyclic voltammetry (CV) experiments were performed on a Bio-Logic SP50 potentiostat. A 3-electrode cell was used, composed of an Au disk

electrode (2 mm diameter), Pt wire counter electrode (1 mm thickness) and a Ag/AgCl pseudo-reference electrode made from Ag wire (0.5 mm thickness) dipped in concentrated $FeCl_3$ to afford a surface layer of AgCl, which was then washed with deionized water and acetone, and dried in vacuo before use. A small volume (3 mL) high-recovery V-vial was used for experimentation. Cell resistances were <500 Ω, and the open circuit potential was checked before each measurement, ensuring ΔV/s <50 mV. All potentials are reported versus the $[Cp_2Fe]^{0/+}$ couple, referenced as internal standard. Solutions utilized in the electrochemical studies were approximately 1 mM in with $[^nPr_4N][BArF_{24}]$ (0.25 M, THF) as supporting electrolyte

CV experiments for compounds $\mathbf{1^{Ce}}$ and $\mathbf{2^{U}}$ were performed using a CH Instruments 600e potentiostat with a PC unit controlled with CHI software (version 13.12). Experiments were performed in a glovebox under an inert N_2 atm using platinum disks (2 mm diameter) embedded in Kel-F thermoplastic as the counter and working electrodes, while the reference electrode consisted of a platinum wire. Solutions utilized in the electrochemical studies were approximately 1 mM in uranium complex with $[NBu_4][PF_6]$ (0.1 M, THF) as supporting electrolyte. All potentials are reported versus the $[Cp_2Fe]^{0/+}$ couple, referenced as internal standard.

X-ray Crystallographic Details

Single crystal X-ray studies for all uranium and cerium complexes reported were carried out on a were collected on a dual source Bruker Venture D8 4-axis diffractometer equipped with a PHOTON II CPAD detector with a IμS Mo Kα X-ray source (α = 0.71073 Å) fitted with a HELIOS MX monochromator at 100(2) K under a flow of nitrogen gas during data collection. The crystals were mounted on a Mitigen Kapton loop coated in NVH oil and maintained at 100(2) K under a flow of nitrogen gas throughout data collection. X-ray studies for reported neptunium and

plutonium complexes were carried out at Los Alamos National Laboratories, in radiologically controlled conditions, on a Bruker AXS SMART APEX II charge-coupled-device diffractometer outfitted with a sealed Mo Kα X-ray source (α = 0.71073 Å), equipped with a graphite monochromatized. Single crystals were coated in NVH oil and mounted inside a 0.5 mm capillary tube which was then sealed under He atmosphere with capillary wax. The capillary was then coated with a thin film of *Hard as Nails*® (polyurethane) to provide structural integrity and add an additional containment layer.[5] Data collection and cell parameter determinations were conducted using the SMART[6] program. Integration of the data and final cell parameter refinements were performed using SAINT[7] software with data absorption correction implemented through SADABS.[8] Structure solutions were completed using direct methods determinations in SHELXTL[9] or Olex2[10] crystallographic packages. All hydrogen atom positions were idealized and treated as riding on the parent atom. CCDC deposit numbers 2238465, 2238466, 2238467, 2238468, 2238469, 2238470, 2238471, 2238472, 2238473 for complexes $\mathbf{1}^{Ce}$, $\mathbf{1}^{Np}$, $\mathbf{2}^{Ce}$, $\mathbf{2}^{Np}$, $\mathbf{2}^{U}$, $\mathbf{3}^{Ce}$, $\mathbf{3}^{Np}$, $\mathbf{3}^{Pu}$ and $\mathbf{3}^{U}$ respectively.

Refinement Special Details

Data for complex $\mathbf{1}^{Np}\cdot Et_2O$ is presented for connectivity purposes only. The diffraction was extremely weak and marred by absorption issues due to local rules which dictate the containment method for crystals. There is no significant diffraction beyond 1.5A. As a result, SIMU restraints were applied to all atoms. Numerous attempts were made to mount the crystals in different oils (Paratone, NVH, Krytox), and the was the only crystal which survived the mounting and sealing process. The bulk characterization data, however, supports the structure depicted. For complexes $\mathbf{2}^{Ce}\cdot$2Hex and $\mathbf{2}^{U}\cdot$2Hex, the two non-coordinated hexane molecules were identified within the unit cell but were severally disordered and were unable to be modeled adequately. Instead, solvent

masking routine "SQUEEZE" was employed to generate a solvent mask which was used to refine against.[11, 12] For $\mathbf{2^{Ce}}$·2Hex, electron density correlating to 2x110 electrons over two voids was removed from the unit cell. For $\mathbf{2^{U}}$·2Hex electron density correlating to 2x115 electrons over two voids was removed from the unit cell. Complex For $\mathbf{2^{U}}$·2Hex, there are two substitutionally disordered solvent molecules (Et_2O/DME) coordinated to K1 which were modeled using a combination of SADI and SIMU restraints. Their occupancies were determined by refining their occupancies freely until their values converged, then setting them fixed at their converged value. For $\mathbf{2^{Ce}}$·2Hex, one of the Et_2O molecules coordinated to K1 possessed positional disorder which was modeled in parts with the use of SADI restrains. For complex $\mathbf{3^{Pu}}$·THF/Et_2O, DELU and SIMU restraints were used to satisfactorily model the disordered of interpenetrated non-coordinated lattice solvents THF and Et_2O. For both $\mathbf{3^{Pu}}$·THF/Et_2O and $\mathbf{3^{U}}$·THF/Et_2O, the ratio of disordered THF/Et_2O were determined by allowing free occupancy refinement of the solvents. For final refinement cycles, they were then fixed to an occupancy which was best fit from the free refinement. Complexes $\mathbf{3^{Pu}}$·THF/Et_2O and $\mathbf{3^{U}}$·THF/Et_2O return alerts ("B level" and "A level" respectively) during the execution of Checkcif validation, related to electron densities near the actinide center (*PLAT972* for $\mathbf{3^{U}}$·THF/Et_2O and P*LAT971* for $\mathbf{3^{Pu}}$·THF/Et_2O), which we attribute to absorption artefacts due to insufficient absorption correction due to the actinide atoms. For complex $\mathbf{3^{Np}}$·Pentane, problems encountered with calculated absorption corrections give rise to a few issues that manifest as *PLAT71/73* "B Level" alerts for residual density. Related to this, the model contains a single carbon atom (C8) which required the use of a ISOR (0.005 0.2) restraint to be applied for anisotropic refinement. Additionally, disorder in the non-coordinated lattice solvent of $\mathbf{3^{Np}}$·Pentane triggers a "B Level" alert of *PLAT360* for shorter than expected C(sp3)-C(sp3) contacts.

Synthesis of $L^{Ar}Np(Cl)(THF)$ ($1^{Np}\cdot Et_2O$) and $[K(DME)_2(L^{Ar})Np(Cl)_2]$ ($2^{Np}\cdot DME$). In a 20 mL glass scintillation vial, $NpCl_4(DME)_2$ (30.0 mg, 54.0 μmol) was added to THF (approx. 0.5 mL) while stirring, forming a light pink solution. The solution was pumped dry in vacuo to a pink oil. The dissolution and drying steps were repeated two more times, then the resulting pink powder was dissolved in 2 mL of THF. To this, while stirring at room temperature, 8.0 mg of potassium graphite (KC_8) was added, resulting in a green/yellow suspension. After 10 mins of stirring, the suspension was filtered via a glass-fiber filter disk, giving a clear yellow filtrate. The filtrate was concentrated in vacuo to ~1 mL THF solution, then hexanes was added to precipitate out a bright yellow powder (putative $NpCl_3(THF)_n$). The near colorless solution was decanted from the yellow powder and the powder was dried. The powder was then dissolved in 2 mL of THF and chilled to –35 °C. Once cold, $[(K(DME)_2)_2L^{Ar}]$ (47.8 mg, 47.3 μmol) was added to the stirring, cold, $NpCl_3(THF)_n$ making a dark brown/red solution. The reaction was left to stir at room temperature for 30 min, then was filtered using a glass-fiber filter disk. The dark brown filtrate was dried completely to a brown paste. The brown paste was then extracted by 5 mL of Et_2O, forming a red solution from the partially soluble solid. The red ether extraction (Fraction "A") was filtered and stored in the freezer at –35 °C. The remaining solid was soluble in THF as well as DME, forming a dark brown solution (Fraction "B"). Single crystals of fraction "A" were grown from the Et_2O solution but were of poor quality. X-ray quality crystals, dark brown needles, were grown from THF solutions of fraction "A" layered with n-hexane and stored at –35 °C for several days (identified as $\mathbf{1}^{Np}\cdot Et_2O$). X-ray quality crystals of fraction "B" (dark red plates) were grown from concentrated DME solution after storage at –35 °C for several weeks (identified as $\mathbf{2}^{Np}\cdot DME$). Yield $\mathbf{1}^{Np}\cdot THF$: 9.8 mg, 19.6%. ^1H NMR (25 °C, 400 MHz, benzene-d_6): δ -8.6 (br s), -7.7 (br s), -3.6 (br s), -2.9 (s), -1.5 (br s), -0.9 (br s), -0.3 (br s), 1.4 (br s) THF, 1.74(br s), 2.9 (br s), 3.6 (br

s) THF, 4.9 (br s), 5.5 (br s), 6.2 (br s), 8.0 (br, s), 10.1 (br s) 10.7 (br s), 11.3 (br s), 16.6 (br s). UV-vis (toluene, 0.14 mM, 25 °C, $L \cdot mol^{-1} \cdot cm^{-1}$): 287 ($\varepsilon$ = 14,536), 321 sh (ε = 1,0352). NIR (toluene, 0.69 mM, 25 °C, $L \cdot mol^{-1} \cdot cm^{-1}$): 652 sh ($\varepsilon$ = 226), 697 sh (ε = 140), 761 (ε = 115), 785 (ε = 132), 806 (ε = 128), 890 (ε = 122), 916 (ε = 137), 945 (ε = 128), 987 (ε = 131), 1025 sh (ε = 145), 1064 (ε = 155), 1276 (ε = 36), 1291 (ε = 35), 1327 (ε = 39), 1348 (ε = 30), 1364 (ε = 30), 1380 (ε = 30), 1404 (ε = 32). Yield $\mathbf{2^{Np}}$·DME: 12.6 mg, 19.5%. ^{1}H NMR (25 °C, 400 MHz, benzene-d_6): δ -21.6 (br s), -20.7 (br s), -102.8 (br s), -2.92 (br d), -1.58 (br s), -0.91(br s), -0.24 (br s), 4.91 (br s), 5.19 (br s), 6.13 (br s), 10.17 (br s), 11.05 (br s), 11.93 (br s), 27.0 (br s). UV-vis-NIR (toluene, 0.5 mM, 25 °C, $L \cdot mol^{-1} \cdot cm^{-1}$): 761 ($\varepsilon$ = 45), 786 (ε = 53), 806 (ε = 38), 885 (ε = 38), 916 (ε = 35), 986 (ε = 36), 1008 sh (ε = 32), 1022 sh (ε = 33), 1077 (ε = 22), 1143 (ε = 13), 1151 (ε = 13), 1278 (ε = 13), 1292 (ε = 12), 1326 (ε = 16).

Synthesis of $L^{Ar}Ce(Cl)(THF)$ ($\mathbf{1^{Ce}}$·Et_2O) and **$[K(DME)(Et_2O)(L^{Ar})Ce(Cl)_2]$** ($\mathbf{2^{Ce}}$·2Hex). In a 20 mL glass scintillation vial, $CeCl_3$ (30.0 mg, 0.122 mmol) was added to 3 mL of THF while stirring, forming a colorless suspension. $[(K(DME)_2)_2L^{Ar}]$ (133.0 mg, 0.130 mmol) was then added to the $CeCl_3$ solution, making a bright orange suspension. The reaction was allowed stir at room temperature and stirred for 16 h, resulting in a slightly turbid orange solution. The mixture was filtered through a plug of Celite supported on a glass frit, passing a clear, orange filtrate. The filtrate was dried under reduced pressure to give a yellow/orange solid. The solid was extracted with Et_2O (5 mL) and moved to a freezer to be stored at –25 °C (Fraction "A"). The remaining solid was dissolved in 2 mL of DME, forming a dark orange solution (Fraction "B"). Fraction "B" was layered with ~ 1 mL of hexanes and stored in the freezer at –25 °C. Fraction "A" grew X-ray quality crystals, as yellow plates, after 24 h and were identified as $\mathbf{1^{Ce}}$·Et_2O. X-ray quality crystals of fraction "B" (orange bocks) were grown from DME solution after storage at –25 °C for 24 h

(identified as $\mathbf{2^{Ce}}$·2Hex). $\mathbf{1^{Ce}}$·Et_2O Yield: 12.1 mg, 10.7%. ^{1}H NMR (25 °C, 400 MHz, benzene-d_6): δ -20.5 (br s), -16.2 (br s), -12.4 (br s), -6.5 (br s), -5.7 (br s), 1.3 (br s), 8.4 (br s), 8.7 (br s), 10.8 (br s), 11.8 (br s), 13.0 (br s), 15.7 (br s), 26.9 (br s), 42.2 (br s). UV-vis (toluene), 0.086 mM, (25 °C, L·mol^{-1}·cm^{-1}): 284 (ε = 32,445), 320 sh (ε = 19,034), 412 v br (ε =1839). Anal. Calcd for $C_{46}H_{54}Cl_1N_2O_1Ce_1$: C, 66.85; H, 6.59; N, 3.39. Found: C, 75.40; H, 7.57; N, 4.08. Duplicate elemental analyses were high in CHN versus calculated, and could be due to the presence of ligand impurities. $\mathbf{2^{Ce}}$·2Hex Yield: 12.2 mg, 9.4%. ^{1}H NMR (25 °C, 400 MHz, benzene-d_6): δ -14.2 (br s), -8.0 (br s), 2.2 (br s) DME, 2.5 (br s) DME, 6.3 (br s), 7.8 (br s), 9.4 (br s), 10.2 (br s), 14.9 (br s,) 18.8 (br s), 25.4 (br s). UV-vis (Toluene), 0.11 mM, (25 °C, L·mol^{-1}·cm^{-1}): 285 (ε = 22,904), 308 sh (ε = 17,415), 426 v br (ε = 1,823). NIR (Toluene), 5.86 mM, (25 °C, L·mol^{-1}·cm^{-1}): 937 (ε = 20), 1078 (ε = 30). Anal. Calcd for $C_{50}H_{66}Cl_2N_2O_4K_1Ce$: C, 59.51; H, 6.59; N, 2.78. Anal. Calcd Found: C, 53.23; H, 6.23; N, 2.35. Elemental analysis was consistently low on carbon content which we attribute to poor combustion characteristics of the compound.

Synthesis of [K(Et$_2$O)$_2$(L^{Ar})U(Cl)$_2$] ($\mathbf{2^{U}}$·2Hex). In a glass 20 mL scintillation vial, UCl_4 (60.0 mg, 0.16 mmol) was added to THF (approx. 3 mL) while stirring, forming a green solution. To this solution, while stirring at room temperature, 24.0 mg of potassium graphite (KC_8) was added, making a deep blue suspension. After 40 mins of stirring, the suspension was filtered via celite, giving a dark blue filtrate. Then, [(K(DME)$_2$)$_2$L^{Ar}] (100.0 mg, 0.10 mmol (1:1 mole ratio based on the assumed production of $UCl_3(THF)_4$ in the previous step) was added to the stirring uranium solution at room temperature, turning the reaction mixture dark brown/red. The reaction was left to stir at room temperature overnight. The reaction mixture became slightly redder after overnight stirring. The reaction mixture was dried completely to a red paste, which was then extracted with 5 – 7 mL Et_2O, forming a red solution and a white/tan precipitate. The reaction was filtered using

a celite padded filter pipette and the dark red filtrate was stored in a freezer at –35 °C. Extracting the Et_2O insoluble solid from the reaction mixture with THF gives a yellow solution which identified in one instance as the 1-D polymeric complex $[L^{Ar}U(Cl)_2(THF)(\mu\text{-}K(THF)_4)]_\infty$ (Figure S2). After 4 days in the freezer, the Et_2O filtrate gave large dark block shaped crystals grew which were X-ray quality and thus identified as $\mathbf{2^U}\cdot$2Hexanes: Yield; 32.5 mg, 28.0%. ^{1}H NMR (25 °C, 300 MHz, benzene-d_6): δ -30.5 (br s), -12.1 (br s), 3.4 (br s), 5.62 (br s), 7.6 (br s), 8.7 (br s), 10.3 (br s), 20.8 (br s), 35.8 (br s), 38.3 (br s). UV-vis (toluene), 0.137 mM, 25 °C, ($L\cdot mol^{-1}\cdot cm^{-1}$): 285 ($\varepsilon$ = 10,506), 319 sh (ε = 6,360), 413 v br (431). NIR (toluene), 0.463 mM, 25 °C, ($L\cdot mol^{-1}\cdot cm^{-1}$): 641 sh ($\varepsilon$ = 347), 692 sh (ε = 266), 762 (236), 974 (ε = 131), 1100 v br (ε = 61), 1268 v br (50). Anal. Calcd. for $C_{50}H_{66}O_4N_2Cl_2U_1K_1$: C, 54.24; H, 6.01; N, 2.53. Found: C, 54.05; H, 6.07; N, 2.45.

Synthesis of $L^{Ar}Ce(I)(THF)$ ($\mathbf{3^{Ce}}\cdot Et_2O$). In a 20 mL glass scintillation vial, CeI_3 (18.0 mg, 0.035 mmol) was added along with 45.0 mg (0.045 mmol) of $[(K(DME)_2)_2L^{Ar}]$, then 3 mL of THF were added making an orange mixture. The mixture was stirred at room temperature for 45 minutes, over which time the reaction became a more homogenous orange solution. The reaction solution was then dried under reduced pressure to an orange paste. Approximately 3 mL of Et_2O was added to the paste, making a turbid orange mixture. The colorless precipitate was removed via filtration through a glass fiber disk, giving a dark orange filtrate. Soon after filtration, small crystals appeared in the filtrate vial. The vial was then moved into a freezer to store at -35 °C for 48 hrs. Large orange needle shaped crystals grew in the vial over the 48 h time period, which were positively identified as $\mathbf{3^{Ce}}\cdot Et_2O$ by single-crystal X-ray diffraction. Yield: 12.3 mg, 17.0%. ^{1}H NMR (25 °C, 400 MHz, benzene-d_6): δ -23.23 (br s), -17.7 (br s), -7.4 (br s), 1.3 (br s), 1.1 (t) Et_2O, 3.2 (m) Et_2O, 8.8 (br s), 9.1 (br s), 11.4 (br s), 13.6 (br s), 14.0 (br s), 16.8 (br s), 29.4 (br s),

46.9 (br s). UV-vis (Toluene), 0.312 mM, 25 °C, L·mol^{-1}·cm^{-1}): 320 (ε = 9,445), 410 (ε = 2,016). Anal. Calcd for $C_{46}H_{54}O_1I_1N_2Ce_1$: C, 60.19; H, 5.93; N, 3.05. Found: C, 75.40; H, 7.57; N, 4.08. Duplicate elemental analyses were high in CHN versus calculated, and could be due to the presence of ligand impurities.

Synthesis of $L^{Ar}U(I)(THF)$ ($\mathbf{3}^{U}$·THF/Et_2O). The previously reported complex $L^{Ar}U(I)(DME)$ can be crystallized as the THF adduct by dissolving 80 mg in 4 mL of THF, followed by drying under vacuum to give a red paste. The paste is subsequently dissolved in 2 mL of Et_2O and then stored in the freezer (–35 °C) for 48 h, resulting in the formation of X-ray quality crystals in the shape of dark red needles in nearly quantitative yield. ^{1}H NMR (25 °C, 400 MHz, benzene-d_6): δ -52.4 (br s), -36.9 (br s), -26.2 (br s), -1.4 (br s), 1.7 (br s) THF, 3.6 (br s) THF, 6.5 (br s), 8.4 (br s), 8.9 (sh br), 10.6 (br s), 12.6 (br s), 16.9 (br s), 26.7 (br s), 28.0(br s), 54.5 (br s), 83.1 (br s). UV-vis (Toluene), 0.254 mM, 25 °C, (L·mol^{-1}·cm^{-1}): 315 (ε = 11,473), 424 (ε = 3,422). NIR (Toluene), 3.00 mM, (25 °C, L·mol^{-1}·cm^{-1}): 683 sh (ε = 653), 759 sh (ε = 560), 800 sh (ε = 488), 963 (ε = 257), 1137 br (ε = 97), 1245 v br (ε = 127). Anal. Calcd for $C_{46}H_{54}O_1I_1N_2U_1$: C, 54.39; H, 5.36; N, 2.76. Found: C, 54.58; H, 5.93; N, 2.62.

Synthesis of $L^{Ar}Np(I)(THF)$ ($\mathbf{3}^{Np}$·Pentane). In a 20 mL glass scintillation vial, $NpI_3(THF)_4$ (13.9 mg, 0.015 mmol) was added along with 16.2 mg (0.016 mmol) of $[(K(DME)_2)_2L^{Ar}]$, then 2 mL of THF were added forming a dark red/brown mixture. The mixture was stirred at room temperature for 30 minutes. Then, the turbid dark red suspension was dried under reduced pressure to a dark red film. The film was extracted in 4 mL of Et_2O, making a turbid red mixture which formed with along with a tan colored pasty solid. The precipitate was removed via filtration through a glass fiber disk, giving a dark red filtrate. The filtrate was concentrated under reduced pressure to

approximately 1 mL in volume and transferred to a 4 mL vial. The 4 mL vial was placed inside of a 20 mL vial and approximately 5 mL of pentanes was added to the outer vial, so that over time the pentanes would diffuse into the Et_2O solution. This vapor diffusion setup was stored in the freezer at –35 °C overnight. Large red crystals in the shape of plates grew in the vial which were of X-ray quality and were positively identified as $\mathbf{3^{Np}}$·Pentane by single-crystal X-ray diffraction. Yield: 4.2 mg, 26.0%. ^{1}H NMR (25 °C, 400 MHz, benzene-d_6): δ -7.4 (br s), -3.0 (br), -0.4 (br s), 7.75 (br s), 11.5 (br s). UV-vis (Toluene), 0.087 mM, (25 °C, L·mol^{-1}·cm^{-1}): 300 (ε = 17,071), 462 (ε = 3,094). NIR (Toluene), 2.13 mM, (25 °C, L·mol^{-1}·cm^{-1}): 747 (ε = 185), 761 (ε = 178), 747 (ε = 185), 761 (ε = 178), 782 (ε = 169), 798 (ε = 161), 818 sh (ε = 126), 842 (ε = 112), 876 br (ε = 106), 894 sh (ε = 95), 914 (ε = 92), 945 (ε = 86), 967 sh (ε = 86), 975 (ε = 91), 993 br (ε = 84), 1,000 br (ε = 83), 1,022 sh (ε = 77), 1,083 sh (ε = 34), 1,210 br (ε = 16), 1,272 (ε = 35), 1,313 (ε = 25), 1,321 (ε = 26), 1,352 br (ε = 26), 1,384 (ε = 24), 1,408 br (ε = 29), 1,436 (ε = 21).

Synthesis of $\mathbf{L^{Ar}Pu(I)(THF)}$ ($\mathbf{3^{Pu}}$·THF/Et_2O). In a 20 mL glass scintillation vial, $PuI_3(THF)_4$ (19.7 mg, 0.022 mmol) was added along with 21.7 mg (0.024 mmol) of $[(K(DME)_2)_2L^{Ar}]$, then 2 mL of THF were added forming red/orange turbid solution. The mixture was stirred at room temperature for 45 minutes. After such time, significant formation of a colorless precipitate was observed. The reaction mixture was dried to a dark red paste under reduced pressure, then extracted with 4-5 mL of $E_{t2}O$, making a turbid red solution. The solution was filtered through a glass-fiber filter disk, giving a deep red filtrate. The precipitate was removed via filtration through a glass-fiber disk, giving a dark red filtrate. The filtrate was concentrated under reduced pressure to approximately 0.5 mL in volume and 1-2 drops of pentane were added. The solution was then moved immediately to a the –35 °C freezer for storage. After 5 days in the freezer, very thin yellow/orange plate shaped crystals grew which were positively identified as $\mathbf{3^{Pu}}$·THF/Et_2O by

single-crystal X-ray diffraction. Yield: 8.4 mg, 35.0% ^{1}H NMR (25 °C, 400 MHz, benzene-d_6): δ -0.8 (br s), -0.4 (br s), -0.3 (br s), 1.2 (br s), 1.4 (br s) THF, 2.7 (br s), 3.6 (br s) THF, 5.9 (br s), 6.4 (br, s), 6.7 (br s), 6.8 (br s), 7.4 (br s), 11.4 (br s). UV-vis (Toluene), 0.010 mM, (25 °C, $L \cdot mol^{-1} \cdot cm^{-1}$): 310 ($\varepsilon$ = 14,100), 436 v br (ε = 1,754). NIR (Toluene), 1.01 mM, (25 °C, $L \cdot mol^{-1} \cdot cm^{-1}$): 675 sh ($\varepsilon$ = 31), 730 (ε = 27), 753 (ε = 30), 791 (ε = 32), 856 sh (ε = 30), 872 (ε = 34), 907 sh (ε = 18), 929 (ε = 22), 943 (ε = 22), 956 (ε = 25), 996 (ε = 29), 1,024 sh (ε = 24), 1,055 (ε = 23), 1,098 sh (ε = 29), 1,107 sh (ε = 23), 1,188 (ε = 82), 1,207 br sh (ε = 30), 1,264 sh (ε = 21), 1,298 sh (ε = 17), 1,397 (ε = 19), 1,430 (ε = 23), 1,455 (ε = 21), 1,558 sh (ε = 26), 1,576 sh (ε = 11).

Table S1. Crystallographic data for $\mathbf{1}^{M}$	$\mathbf{1}^{Np}\cdot Et_2O$	$\mathbf{1}^{Ce}\cdot Et_2O$
	$L^{Ar}Np(Cl)(THF)\cdot Et_2O$	$L^{Ar}Ce(Cl)(THF)\cdot Et_2O$
empirical formula	$C_{50}H_{64}N_2O_2ClNp$	$C_{50}H_{64}N_2O_2ClCe$
crystal habit, color	Plate, dark brown	block, orange
crystal size (mm)	0.1 × 0.1 × 0.01	0.12 × 0.1 × 0.1
crystal system	Triclinic	Triclinic
space group	$P\bar{1}$	$P\bar{1}$
volume (Å^3)	2283.2(7)	2212.12(9)
a (Å)	10.809(1)	10.5933(2)
b (Å)	13.816(1)	13.7861(4)
c (Å)	17.097(3)	16.9187(4)
α (deg)	78.95(1)	78.826(1)
β (deg)	73.61(1)	73.728(1)
γ (deg)	69.59(1)	69.733(1)
Z	2	2
formula weight (g/mol)	997.51	900.62
density (calculated) (mg/m^3)	1.343	1.351
absorption coefficient (mm^{-1})	2.366	1.130
F_{000}	924.0	937.0
total no. reflections	30922	69199
unique reflections	8223	20123
final *R* indices [$I > 2\sigma(I)$]	$R_1 = 0.0722$, $wR_2 = 0.01519$	$R_1 = 0.0350$, $wR_2 = 0.0714$
largest diff. peak and hole (e$^-$ Å^{-3})	–1.60 and 0.86	-0.98 and 1.87
GOF	0.989	1.040

Table S2. Crystallographic data for $\mathbf{2^M}$	$\mathbf{2^{Np}}$·DME $[K(DME)_2(L^{Ar})Np(Cl)_2]$·DME	$\mathbf{2^{Ce}}$·2Hex $[K(DME)_{0.5}(Et_2O)_{1.5}(L^{Ar})Ce(Cl)_2]$ ·2Hex	$\mathbf{2^{U}}$·2Hexane $[K(Et_2O)_2(L^{Ar})U(Cl)_2]$·2Hex
empirical formula	$C_{54}H_{75}N_2O_6Cl_2KNp$	$C_{56}H_{80}N_2O_{2.5}Cl_2KCe$	$C_{62}H_{86}N_2O_2Cl_2KU$
crystal habit, color	Bock, dark brown	Plate, orange	Block, red
crystal size (mm)	0.2 × 0.2 × 0.1	0.12 × 0.1 × 0.1	0.4 × 0.4 × 0.3
crystal system	Monoclinic	Monoclinic	Monoclinic
space group	$P2_1/c$	$P2_1/c$	$P2_1/c$
volume (Å^3)	5471.4(7)	5824.8(3)	5811.0(1)
a (Å)	17.930(1)	13.35624(4)	13.343(1)
b (Å)	12.0060(7)	16.9877(5)	16.986(1)
c (Å)	26.706(1)	25.6828(8)	25.645(3)
α (deg)	90	90	90
β (deg)	107.882(8)	90.9300(10)	91.263(4)
γ (deg)	90	90	90
Z	4	2	4
formula weight (g/mol)	1195.16	1071.36	1239.39
density (calculated) (mg/m^3)	1.451	1.123	1.229
absorption coefficient (mm^{-1})	2.121	0.978	2.989
F_{000}	2428.0	2042.0	2163.0
total no. reflections	35831	240020	34546
unique reflections	11123	17795	17753
final *R* indices [$I > 2\sigma(I)$]	$R_1 = 0.0448$, $wR_2 = 0.0796$	$R_1 = 0.0417$, $wR_2 = 0.0930$	$R_1 = 0.0474$, $wR_2 = 0.00808$
largest diff. peak and hole (e$^-$ Å^{-3})	–0.62 and 1.45	-1.28 and 1.47	-2.76 and 1.35
GOF	1.002	1.085	1.121

Table S3. Crystallographic data for $\mathbf{3^{M}}$	$\mathbf{3^{Np}}\cdot$Pentane	$\mathbf{3^{Ce}}\cdot Et_2O$	$\mathbf{3^{U}}\cdot THF_{0.8}Et_2O_{0.2}$	$\mathbf{3^{Pu}}\cdot THF_{2/3}Et_2O_{1/3}$
	L^{Ar}Np(I)(THF)·Pent	L^{Ar}Ce(I)(THF)·Et_2O	L^{Ar}U(I)(THF)·$THF_{0.8}/Et_2O_{0.2}$	L^{Ar}Pu(I)(THF)·$THF_{2/3}/Et_2O_{1/3}$
empirical formula	$C_{51}H_{66}IN_2ONp$	$C_{50}H_{64}IN_2O_2Ce$	$C_{50}H_{63}IN_2O_2U$	$C_{50}H_{63}IN_2O_2Pu$
crystal habit, color	Plate, dark red	Needle, yellow	Needle, red	Plate, Orange
crystal size (mm)	0.3 × 0.4 × 0.8	0.12 × 0.1 × 0.1	0.2 × 0.1 × 0.1	0.7 × 0.3 × 0.2
crystal system	Monoclinic	Monoclinic	Monoclinic	Monoclinic
space group	$P2_1/c$	$P2_1/n$	$P2_1/c$	$P2_1/c$
volume (Å^3)	5471.4(7)	4428.9(3)	4479.5(5)	4511.6(6)
a (Å)	17.930(1)	11.4528(4)	13.779(8)	13.8050(10)
b (Å)	12.0060(7)	21.5419(9)	15.6184(10)	15.6334(12)
c (Å)	26.706(1)	18.1661(7)	21.8752(13)	21.9877(18)
α (deg)	90	90	90	90
β (deg)	107.882(8)	98.817(2)	107.8970(10)	108.057(3)
γ (deg)	90	90	90	90
Z	4	4	4	4
formula weight (g/mol)	1086.98	992.05	1088.35	1099.95
density (calculated) (mg/m^3)	1.451	1.488	1.614	1.609
absorption coefficient (mm^{-1})	2.121	1.488	4.353	2.185
F_{000}	2428.0	2020.0	2150.0	2159.0
total no. reflections	35831	75264	134834	182029
unique reflections	11123	13549	13721	11214
final *R* indices [$I > 2\sigma(I)$]	R_1 = 0.0448, wR_2 = 0.0796	R_1 = 0.0303, wR_2 = 0.0704	R_1 = 0.0161, wR_2 = 0.0353	R_1 = 0.0377, wR_2 = 0.0985
largest diff. peak and hole (e$^-$ Å^{-3})	–0.62 and 1.45	-1.06 and 0.72	-0.63 and 0.79	–2.46 and 2.83
GOF	1.002	1.097	1.039	1.046

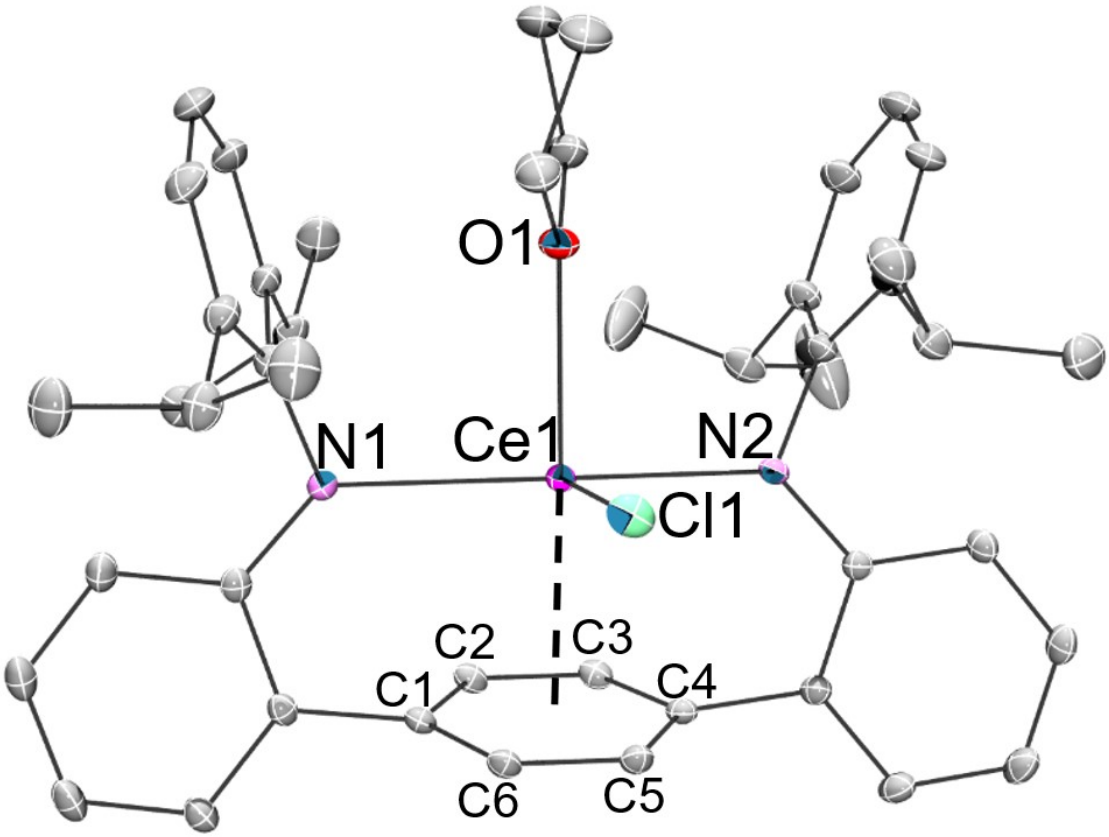

Figure S1. ORTEP diagram of $\mathbf{1}^{Ce}\cdot Et_2O$ with 50% probability thermal ellipsoids. Hydrogen atoms and co-crystalized solvent are omitted for clarity.

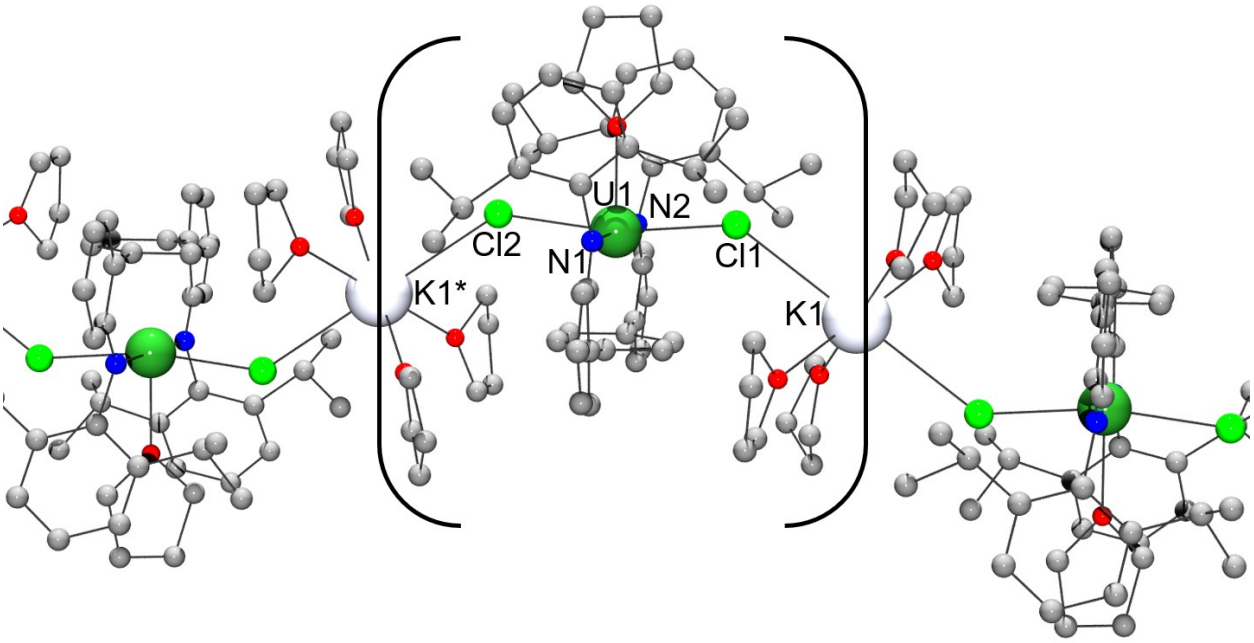

Figure S2. Ball and stick model of $[L^{Ar}U(Cl)_2(THF)(\mu\text{-}K(THF)_4)]_\infty$ shown for connectivity purposes only. A section of the polymeric chain is illustrated, with the asymmetric unit bracketed for reference. Hydrogen atoms are omitted for clarity.

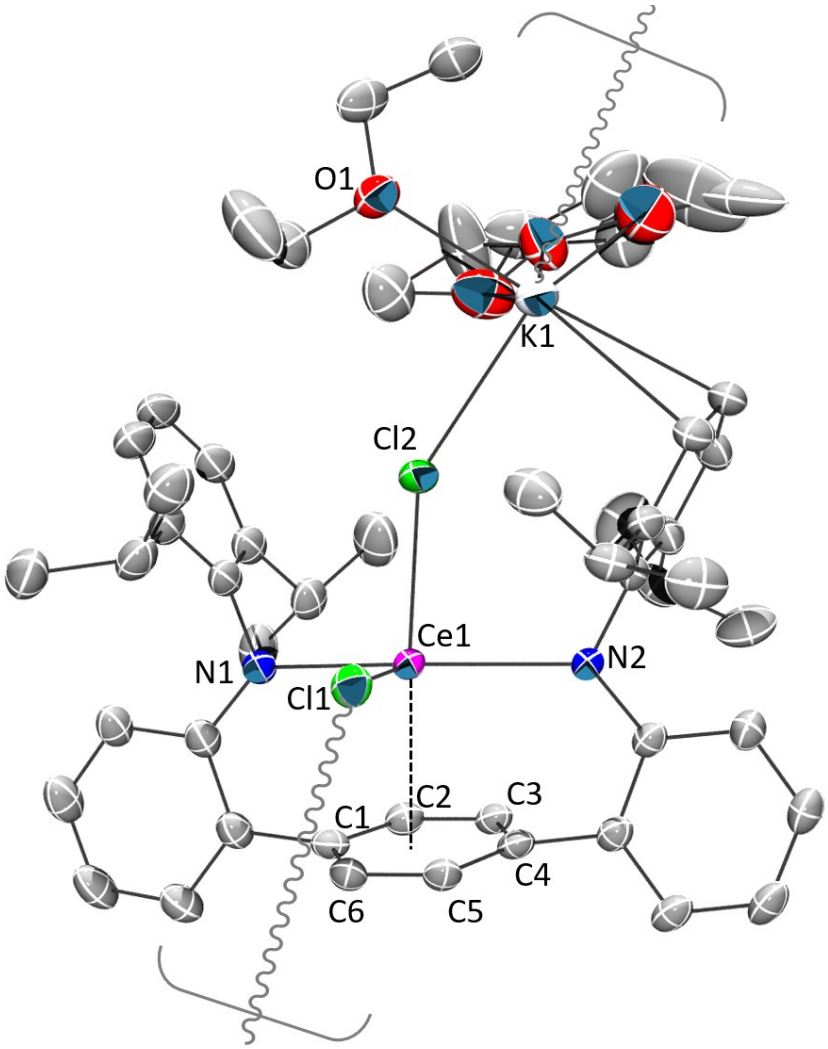

Figure S3. ORTEP diagram of the asymmetric unit of **2**^{Ce}·2Hex with 50% probability thermal ellipsoids. Hydrogen atoms and co-crystalized solvent are omitted for clarity. Note there is substitutional disorder with both DME and Et_2O sharing one of the coordination positions of K1 in a 50:50 ratio, both are shown in this figure. Direction of polymeric chain growth is indicated by bracketed squiggly lines.

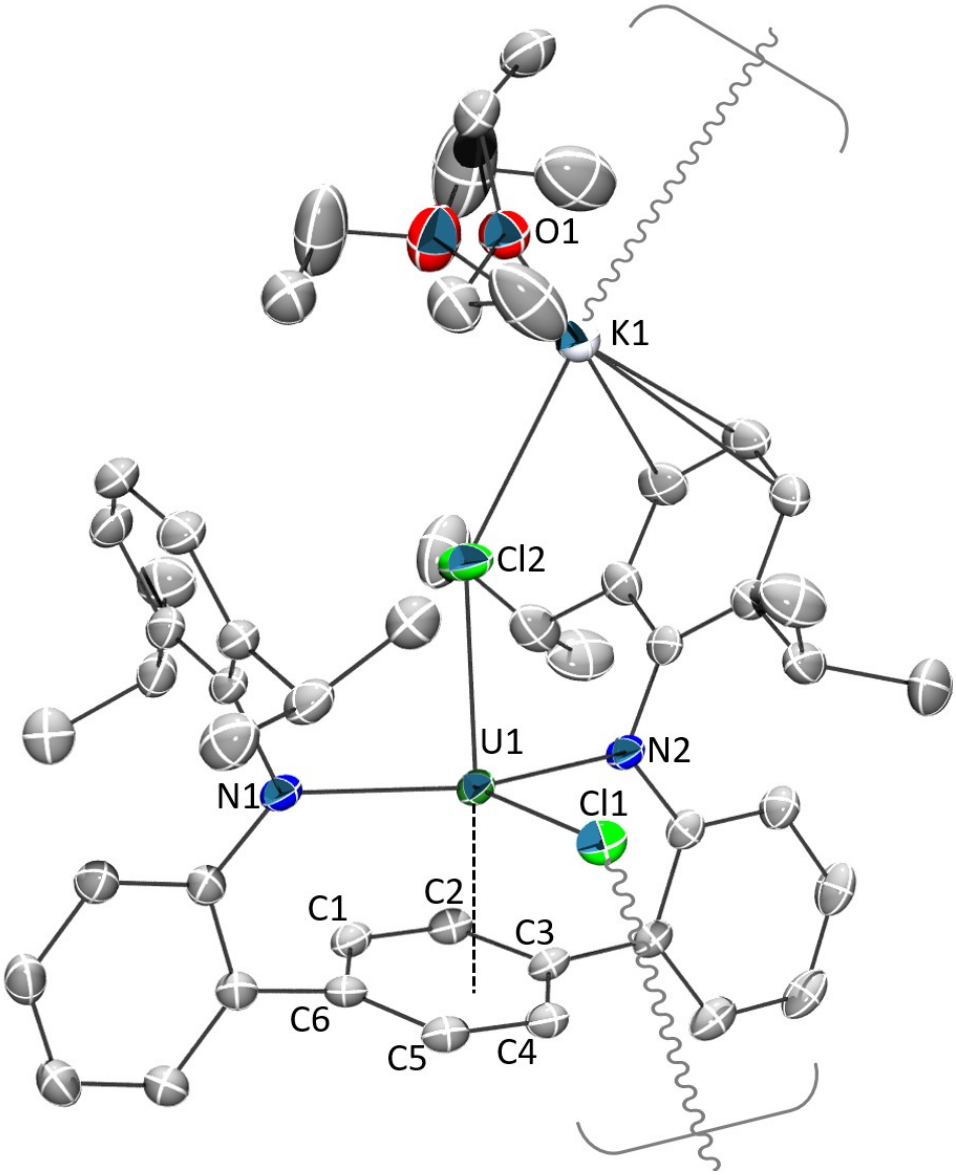

Figure S4. ORTEP diagram of the asymmetric unit of $\mathbf{2}^{\mathbf{U}}$·2Hexane with 50% probability thermal ellipsoids. Hydrogen atoms and co-crystalized solvent are omitted for clarity. Direction of polymeric chain growth is indicated by bracketed squiggly lines.

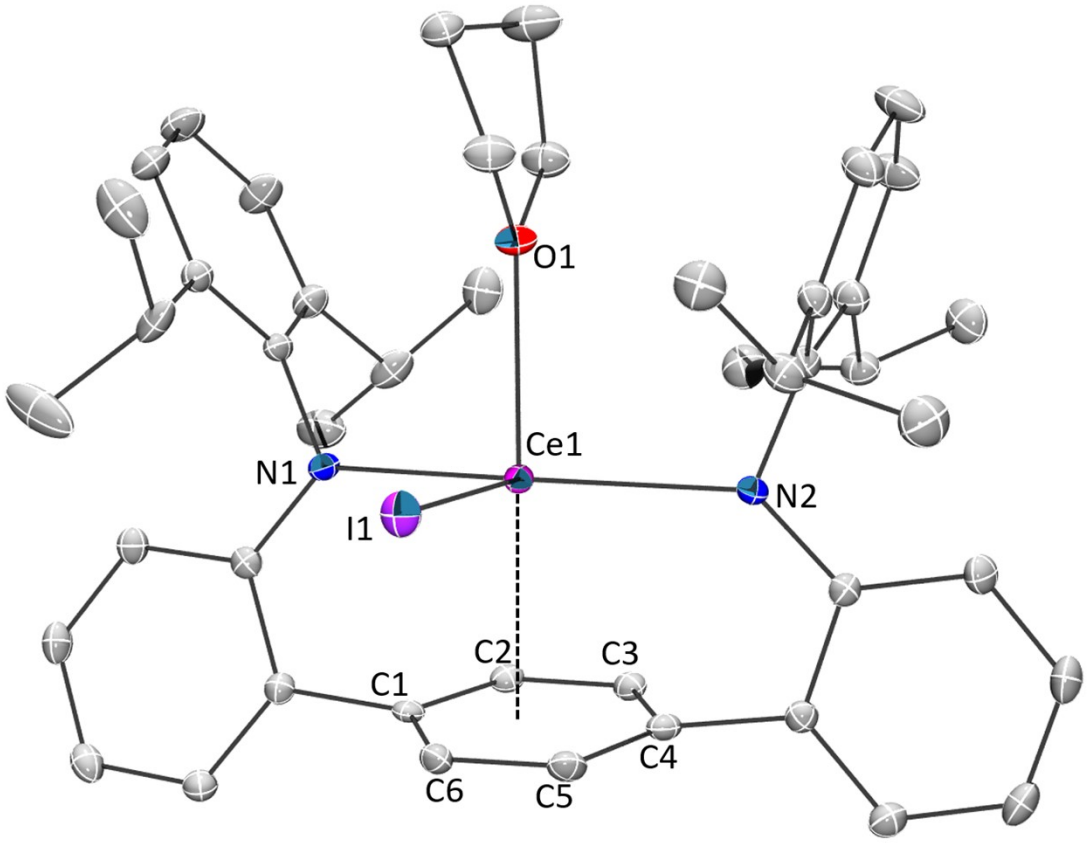

Figure S5. ORTEP diagram of $\mathbf{3}^{Ce}\cdot Et_2O$ with 50% probability thermal ellipsoids. Hydrogen atoms and co-crystalized solvent are omitted for clarity.

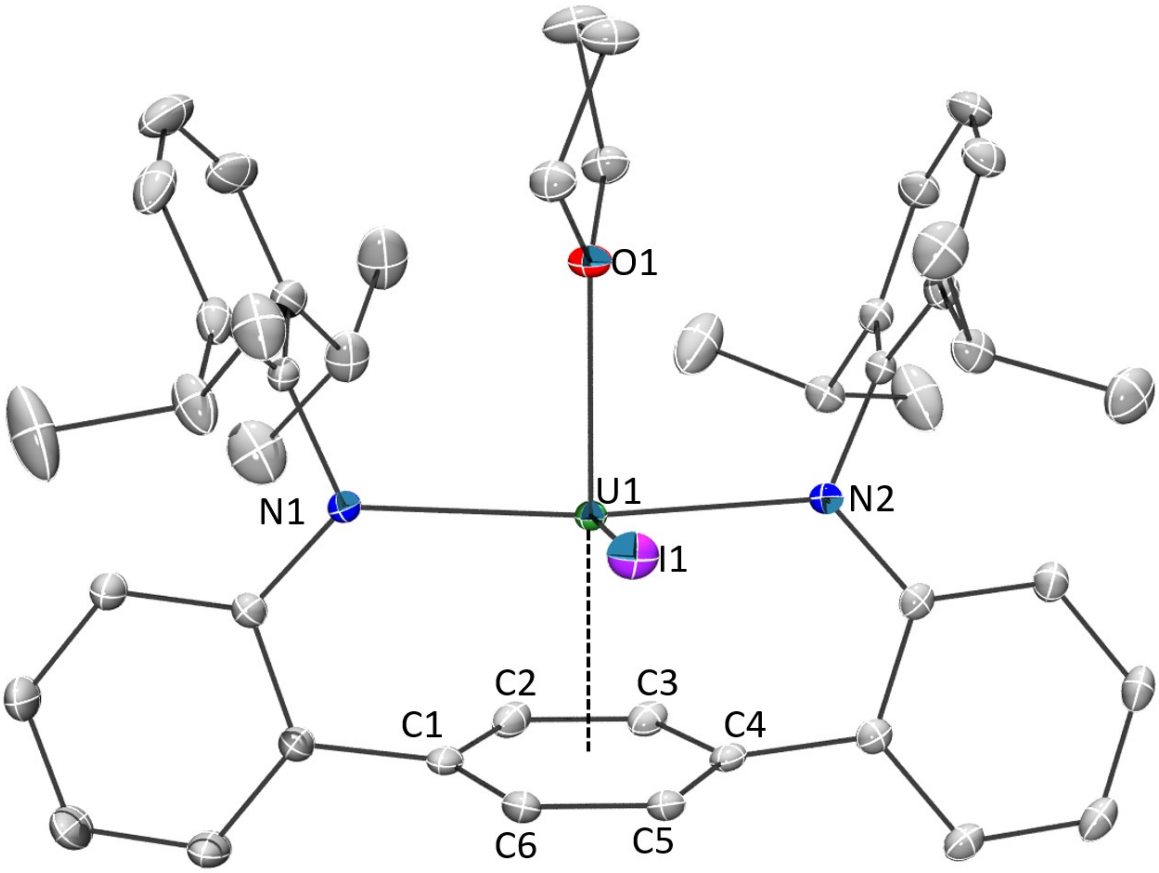

Figure S6. ORTEP diagram of $\mathbf{3^U}$·THF/Et_2O with 50% probability thermal ellipsoids. Hydrogen atoms and co-crystalized solvent are omitted for clarity.

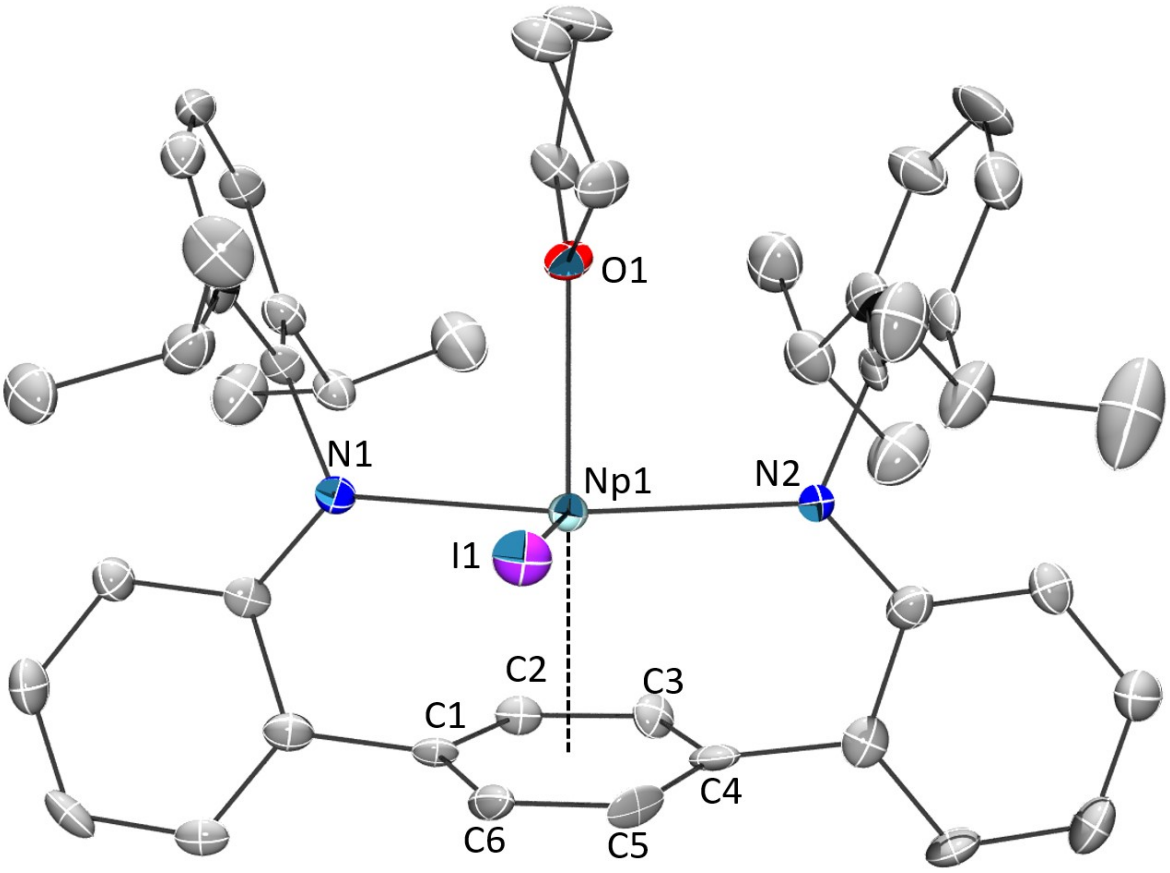

Figure S7. ORTEP diagram of $\mathbf{3}^{\mathbf{Np}}$·Pent with 50% probability thermal ellipsoids. Hydrogen atoms and co-crystalized solvent are omitted for clarity.

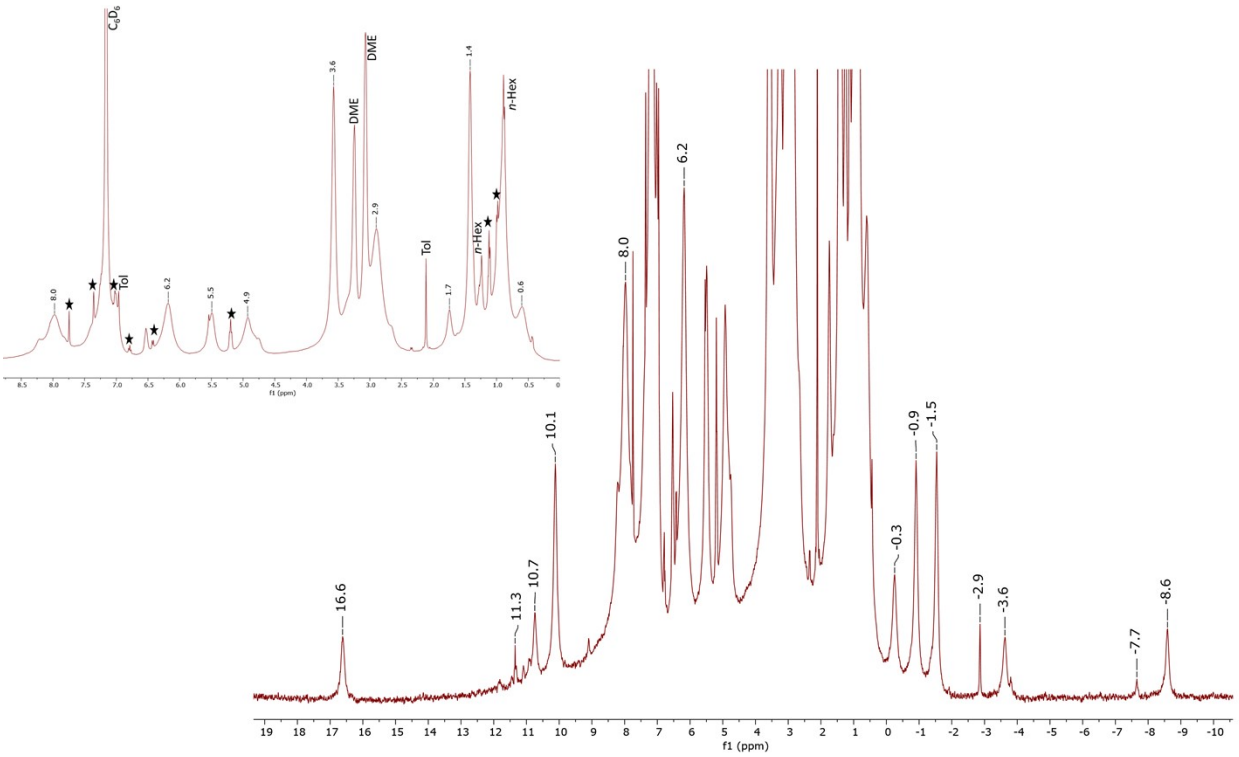

Figure S8. Baseline corrected ^{1}H NMR spectrum of **1**$^{\mathbf{Np}}$ in benzene-d_6 at 25 °C. Insert shows diamagnetic region with H-ligand impurity labeled by star symbol.

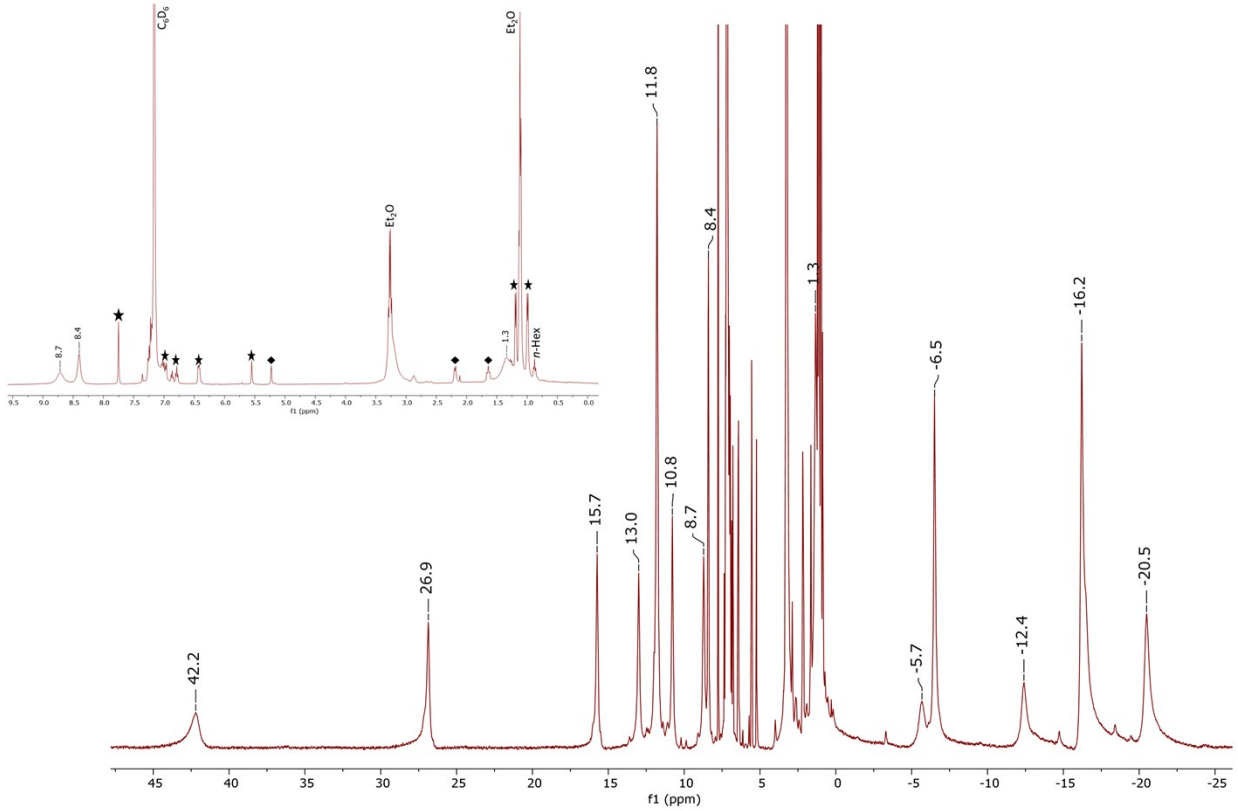

Figure S9. ^{1}H NMR spectrum of **1**$^{\mathbf{Ce}}$ in benzene-d_6 at 25 °C. Insert shows diamagnetic region with H-ligand impurity labeled by star symbol. Dimond symbol indicates unknown impurity.

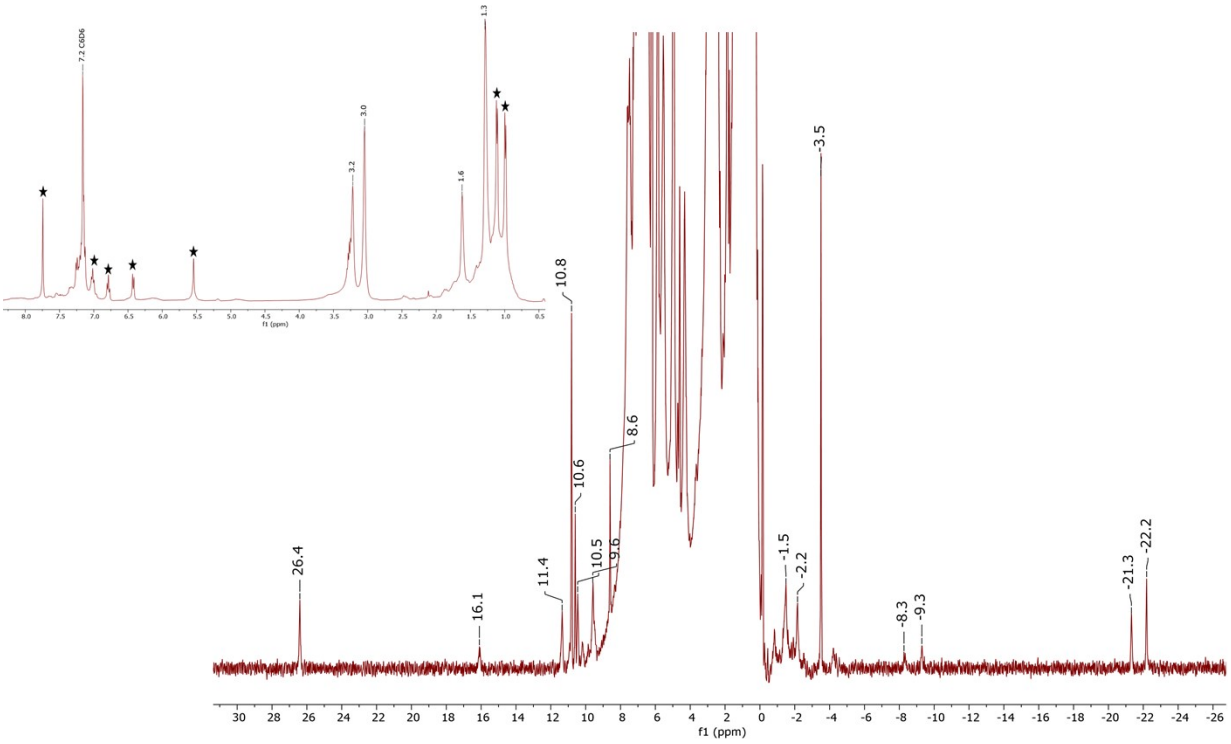

Figure S10. ^{1}H NMR spectrum of $\mathbf{2^{Np}}$ in benzene-d_6 at 25 °C**.** Insert shows diamagnetic region with H-ligand impurity labeled by star symbol.

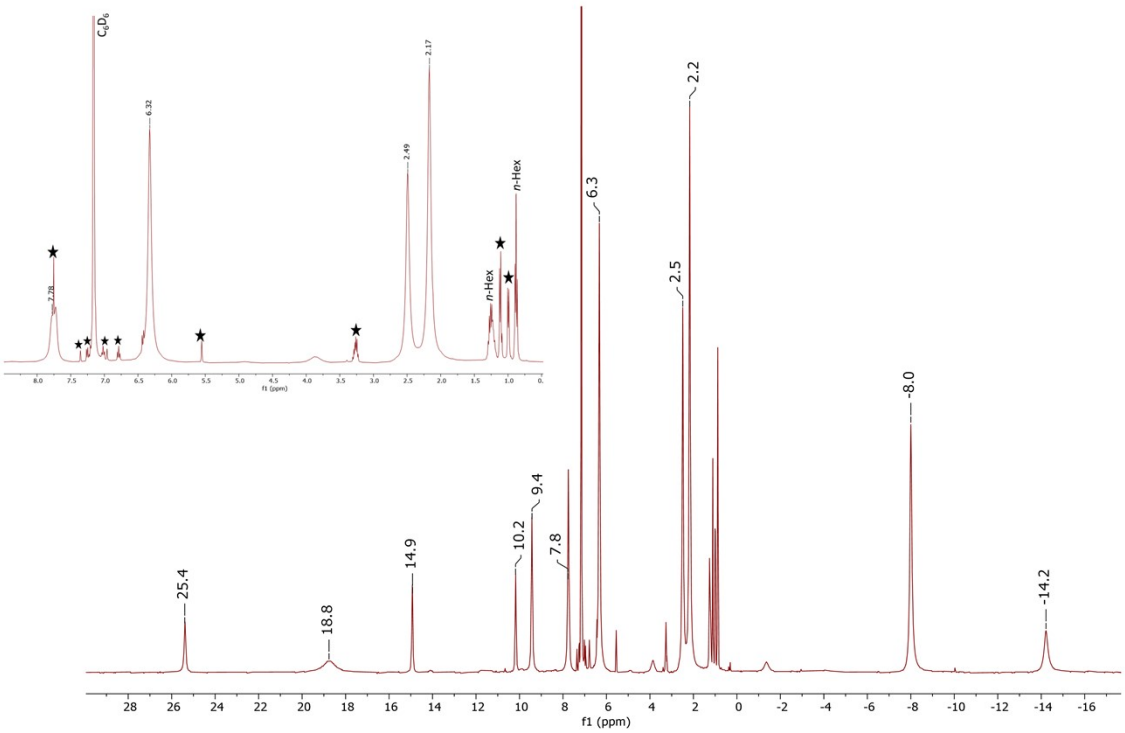

Figure S11. ^{1}H NMR spectrum of **2^{Ce}** in benzene-d_6 at 25 °C**.** Insert shows diamagnetic region with H-ligand impurity labeled by star symbol.

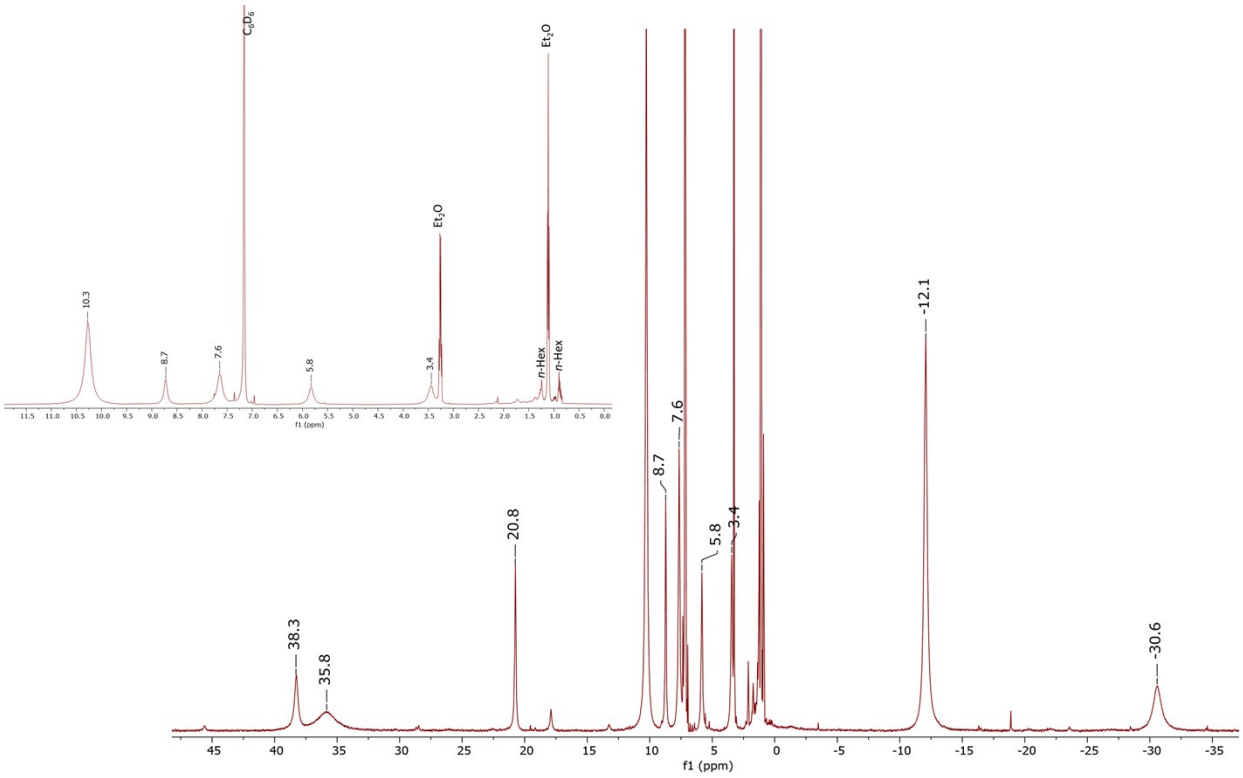

Figure S12. Baseline uncorrected ^{1}H NMR spectrum of $\mathbf{2}^{\mathbf{U}}$ in benzene-d_6 at 25 °C. Insert shows diamagnetic region.

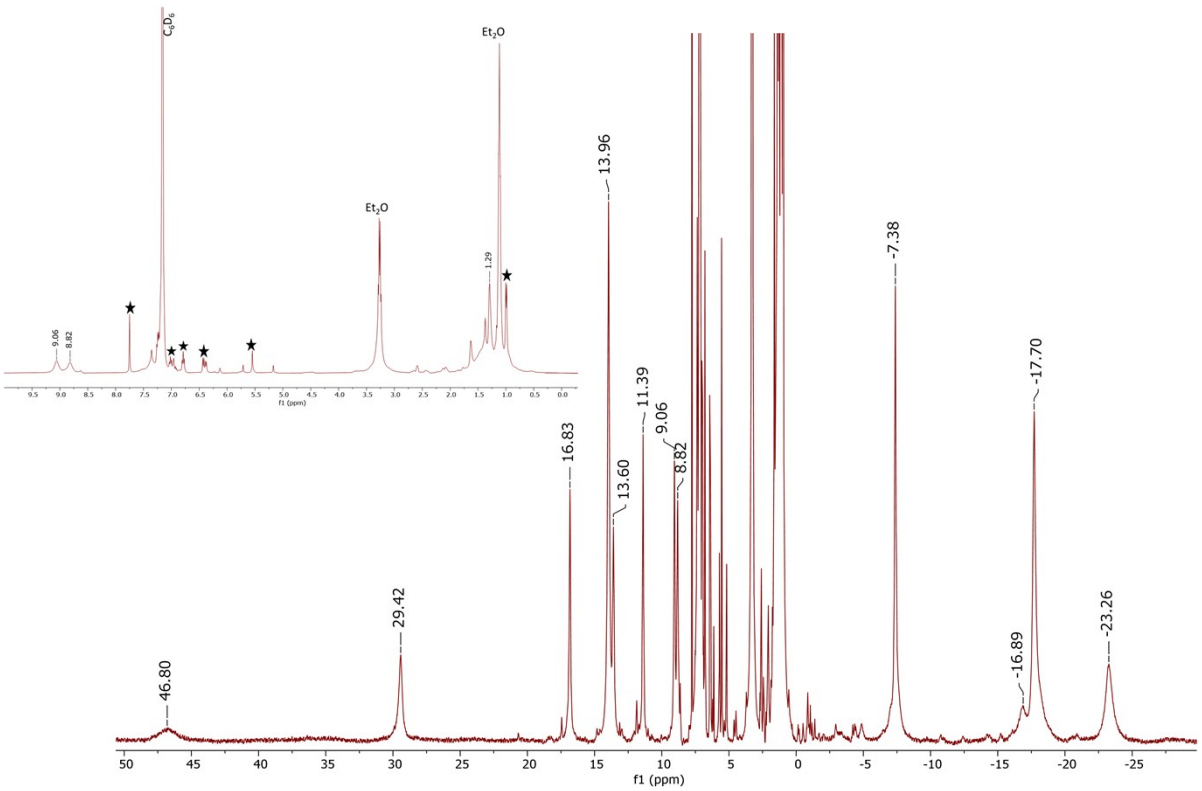

Figure S13. ^{1}H NMR spectrum of $\mathbf{3^{Ce}}$ in benzene-d_6 at 25 °C. Insert shows diamagnetic region with H-ligand impurity labeled by star symbol.

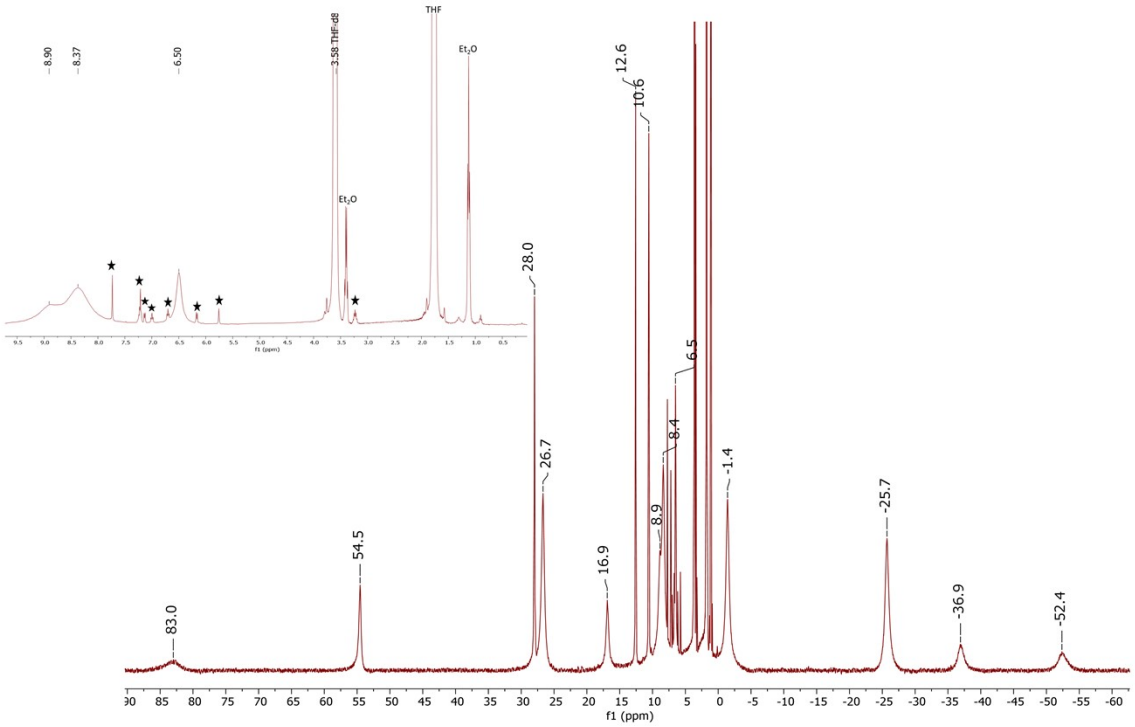

Figure S14. ^{1}H NMR spectrum of $\mathbf{3}^{\mathbf{U}}$ in benzene-d_6 at 25 °C. Insert shows diamagnetic region with H-ligand impurity labeled by star symbol.

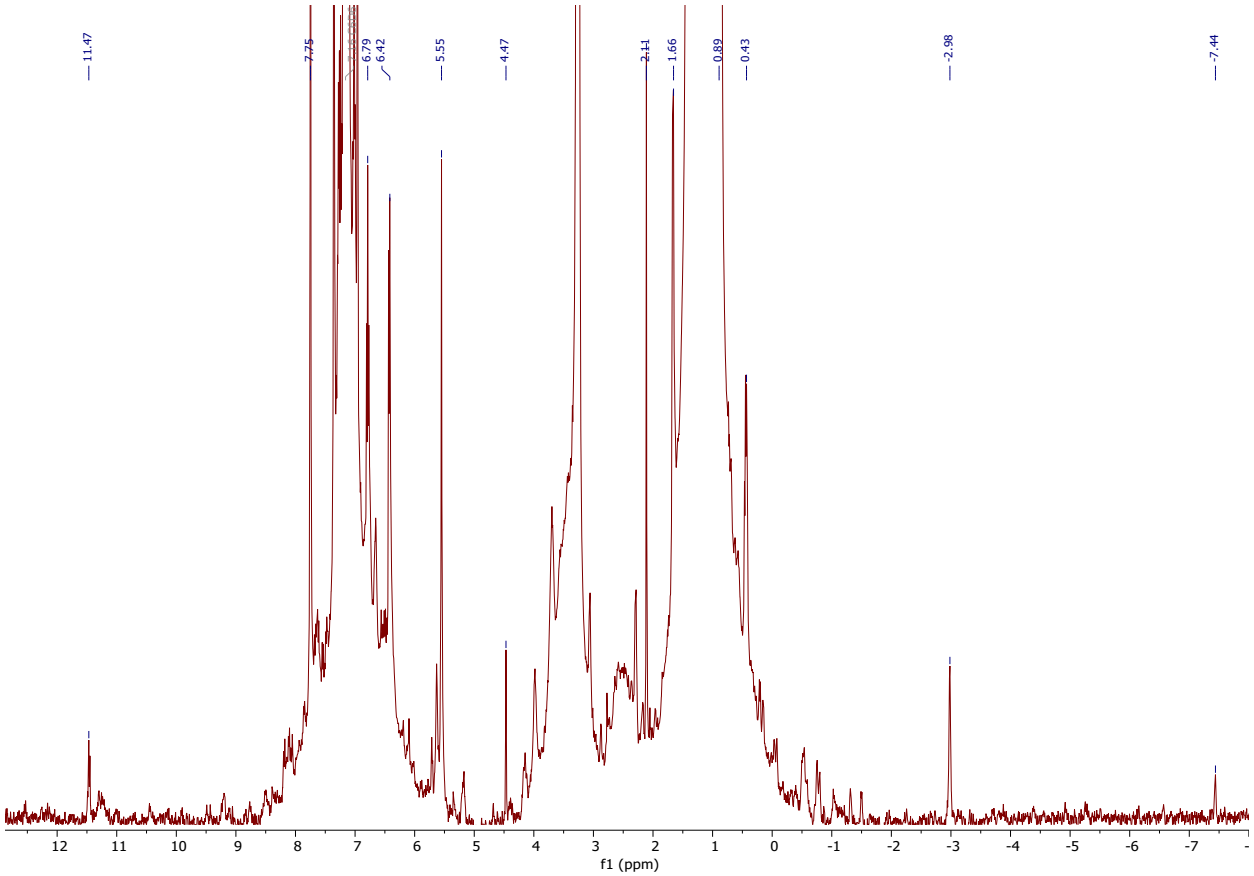

Figure S15. ^{1}H NMR spectrum of $\mathbf{3^{Np}}$ in benzene-d_6 at 25 °C**.**

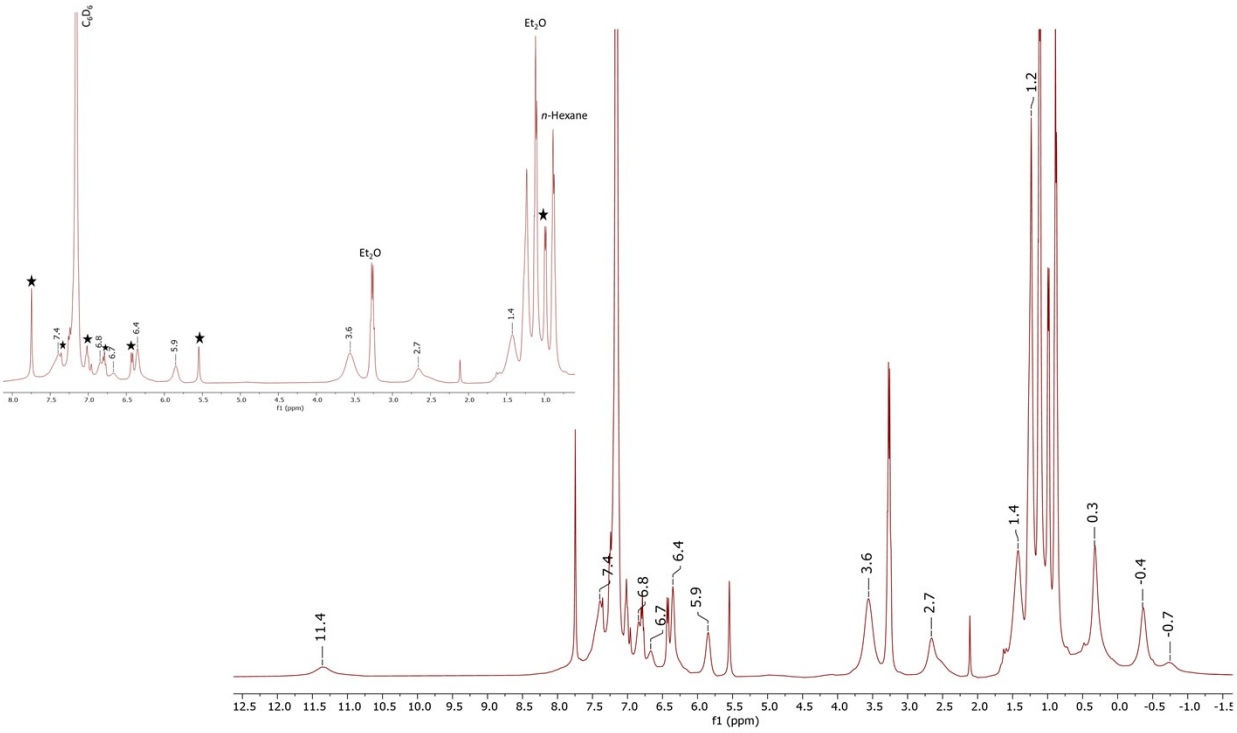

Figure S16. ^{1}H NMR spectrum of **3^{Pu}** in benzene-d_6 at 25 °C**.** Insert shows diamagnetic region with H-ligand impurity labeled by star symbol.

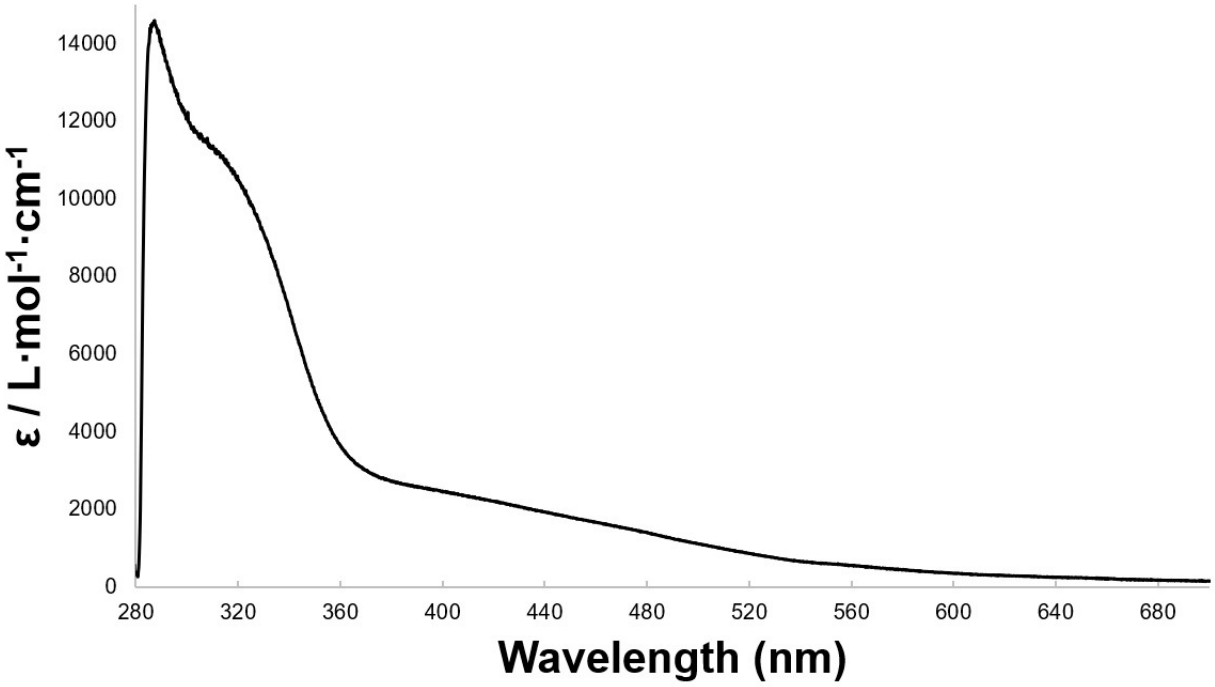

Figure S17. Room temperature electronic absorption spectra of $\mathbf{1^{Np}}$ (0.14 mM in toluene).

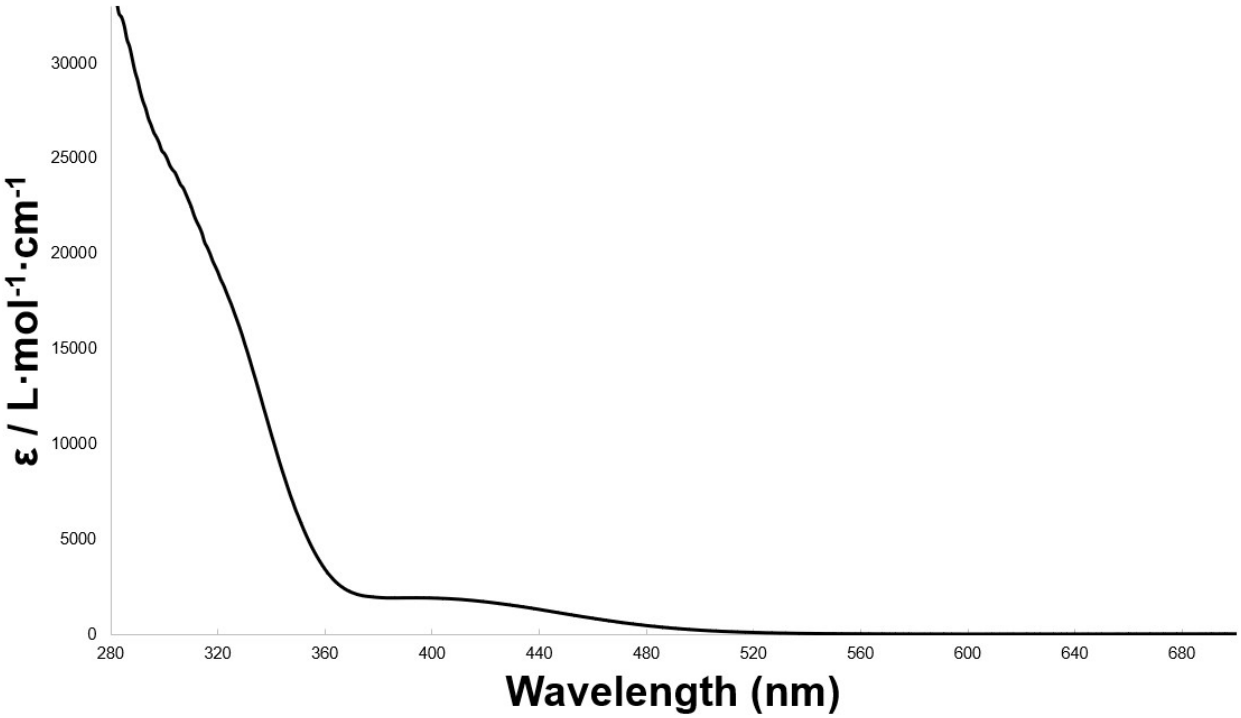

Figure S18. Room temperature electronic absorption spectra of $\mathbf{1}^{Ce}$ (0.08 mM in THF).

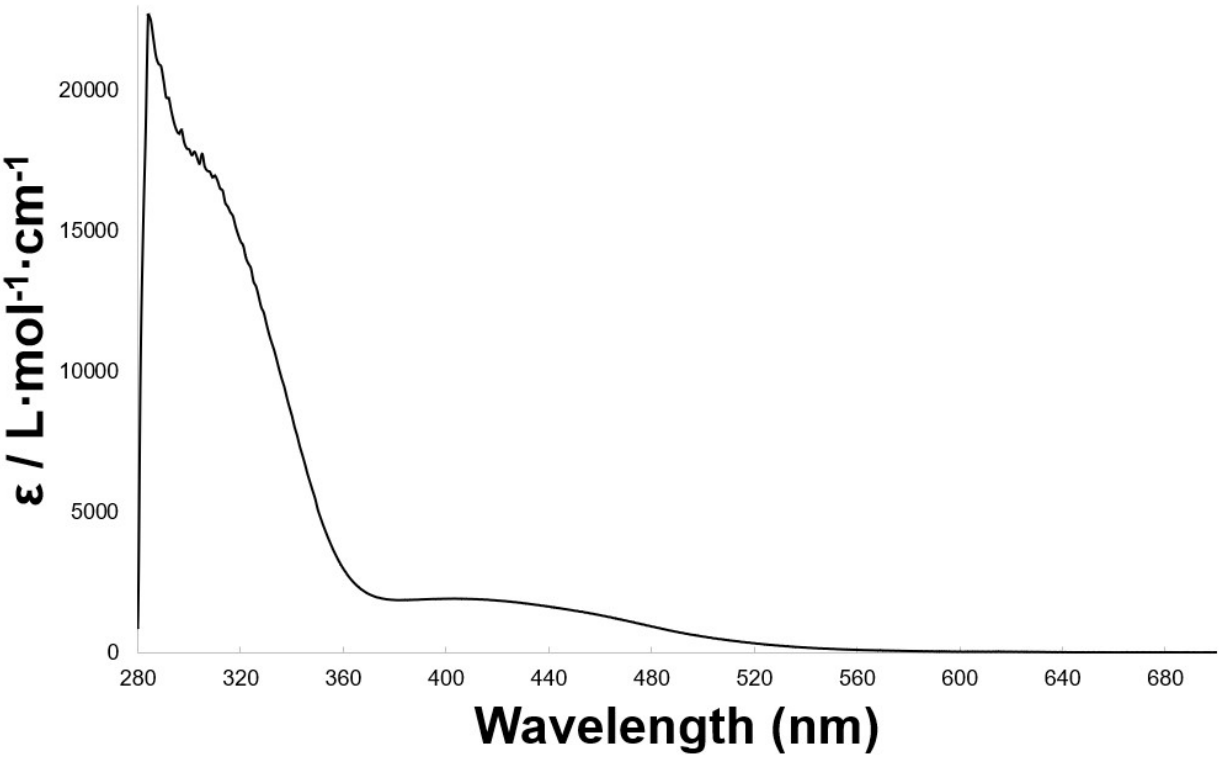

Figure S19. Room temperature electronic absorption spectra of $\mathbf{2}^{\mathbf{Ce}}$ (0.11 mM in THF).

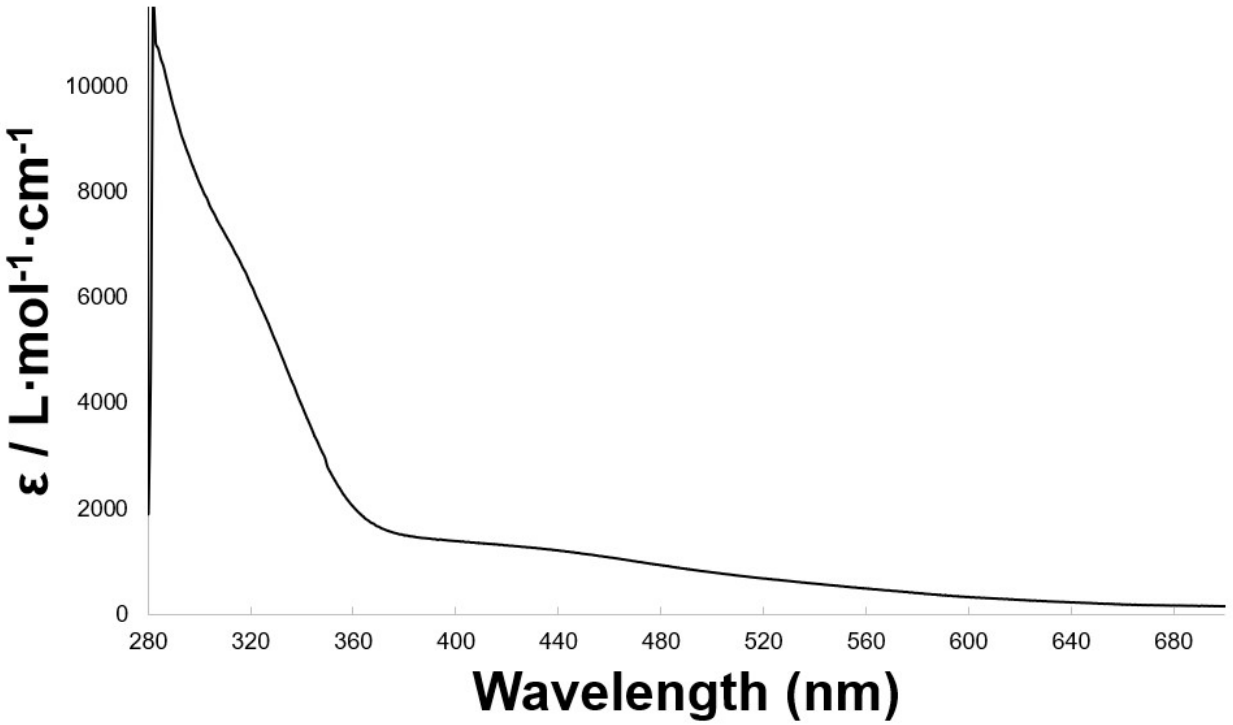

Figure S20. Room temperature electronic absorption spectra of $\mathbf{2}^{U}$ (0.10 mM in THF).

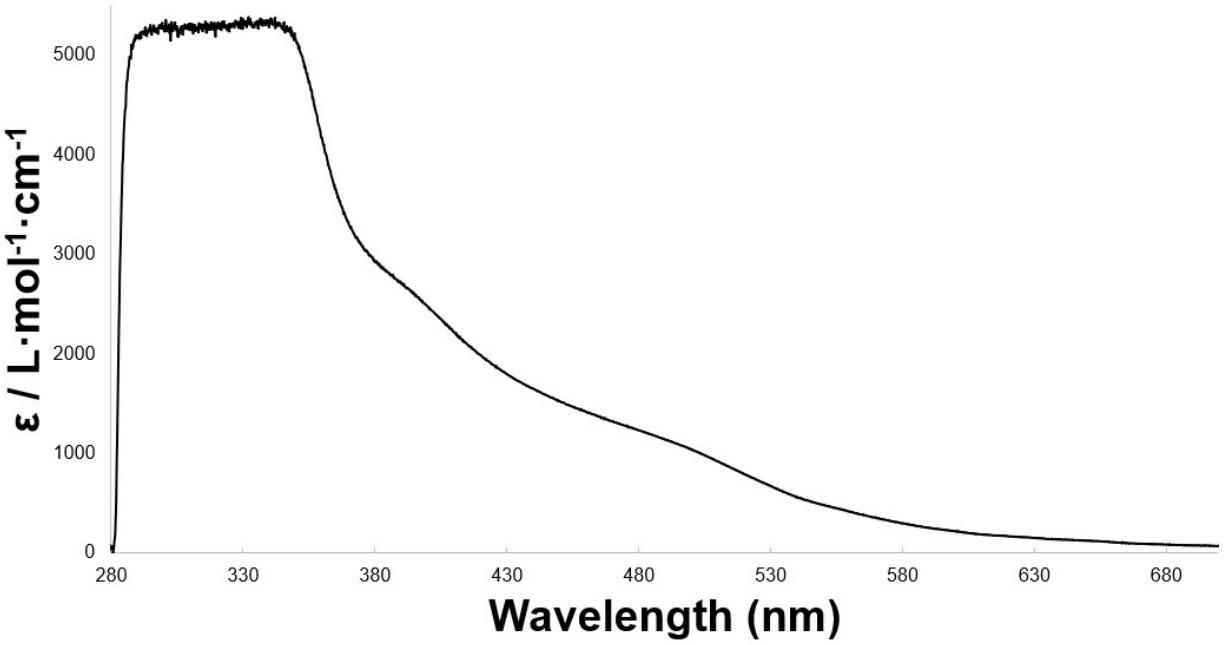

Figure S21. Room temperature electronic absorption spectra of $\mathbf{2^{Np}}$ (0.50 mM in toluene). *Detector reached saturation conditions near 350 nm, due to limited quantity of $\mathbf{2^{Np}}$, no additional spectra at lower concentrations were possible.

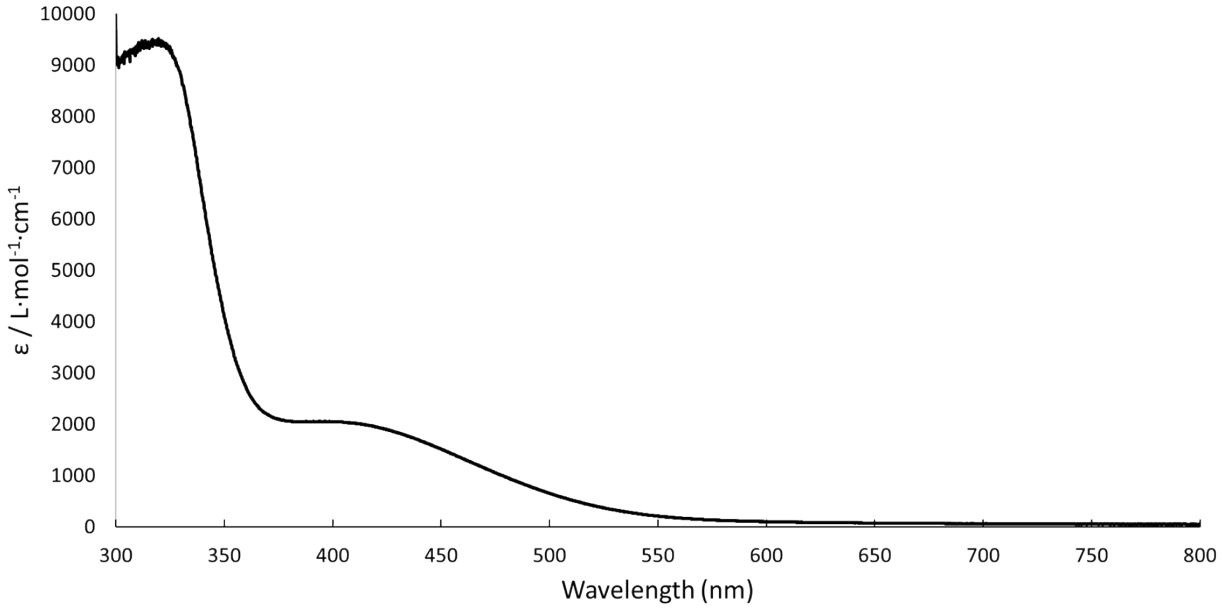

Figure S22. Room temperature electronic absorption spectra of **3**^{Ce} (0.31 mM in toluene).

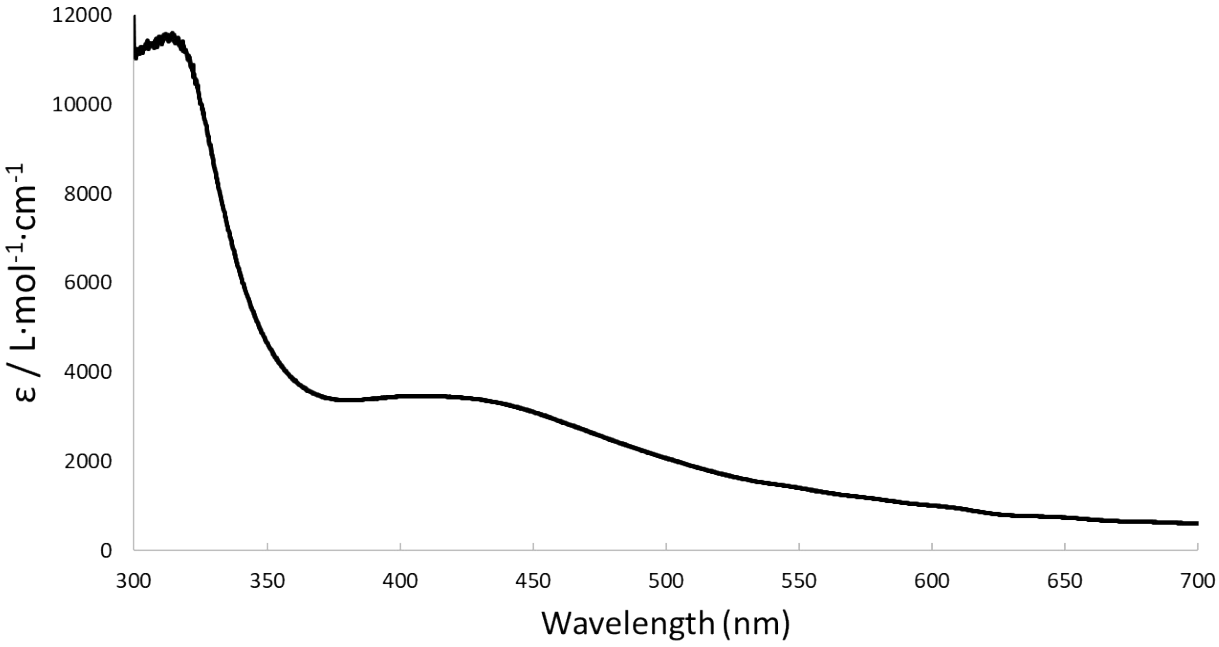

Figure S23. Room temperature electronic absorption spectra of $\mathbf{3^U}$ (0.25 mM in THF).

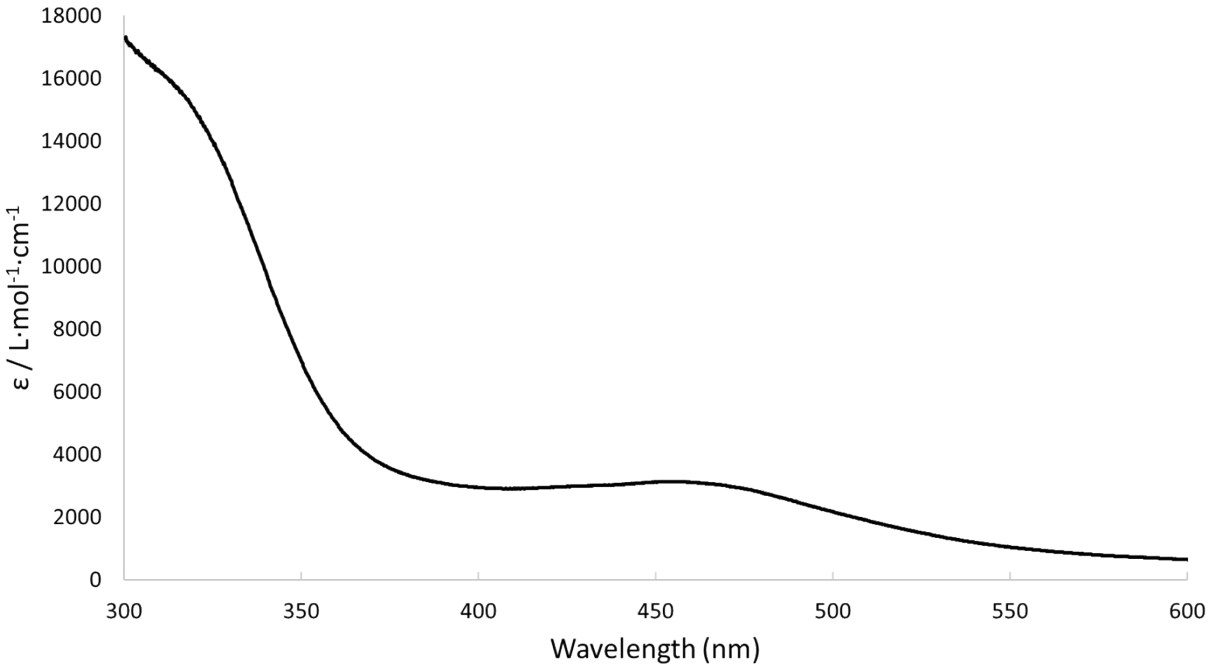

Figure S24. Room temperature electronic absorption spectra of **3^{Np}** (0.09 mM in toluene).

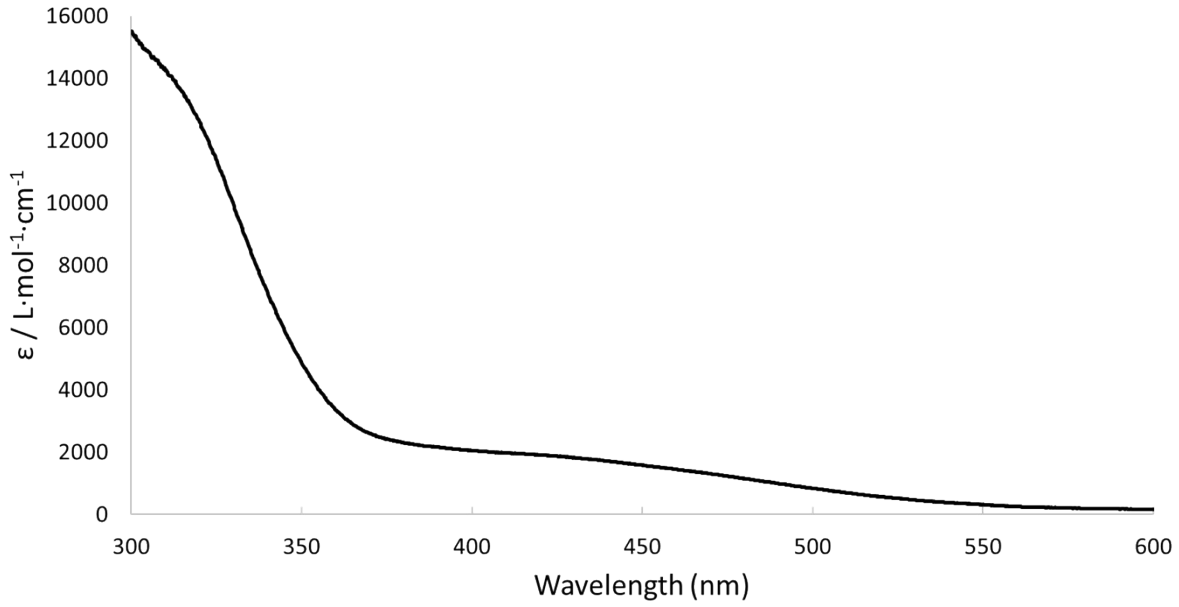

Figure S25. Room temperature electronic absorption spectra of **3^{Pu}** (0.097 mM in THF).

Table S4. Selected bond metrics for $\mathbf{1^{M}}$ complexes. *Note that the metrical data taken from the structure solution for $\mathbf{1^{Np}}$ should be considered in the context of the poor quality of the data (see "Special Refinement Details") and not used for metrical comparison purposes (connectivity only).

Complex	M-N Bond Distances (Å)	M-Cent Distance (Å)	M-η⁶-C Range (Å)	M-Cl Distance (Å)	N-M-N Bond Angle (°)	Shannon 6-coord. Ionic Radii (Å) of M^{3+} ions
$\mathbf{1^{Ce}}\cdot Et_2O$	2.471(1)/2.503(1)	2.6698(7)	2.960(4)-3.116(4)	2.6378(4)	156.15(4)	1.01
$\mathbf{1^{Np}}\cdot Et_2O$	2.47(1)/2.50(1)*	2.600(5)*	2.92(1)-3.00(1)*	2.586(3)*	156.3(1)*	1.01*

Table S5. Distortion of the planarity of the C_{aryl} ring, viz. bending of ipso-substituents (C7-C_{cent}-C13) for complexes $\mathbf{2^M}$ and $\mathbf{3^M}$.

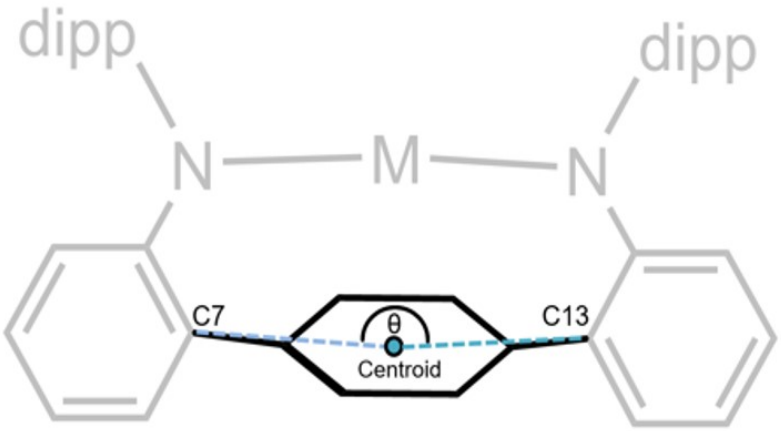

Complex	*Ipso*-substituents (°)	Avg. C-C_{aryl} Bond Distances (Å)
$\mathbf{2^{Ce}}$·2Hex	172.24(8)	1.40
$\mathbf{2^{U}}$·2Hex	172.46(11)	1.40
$\mathbf{2^{Np}}$·DME	171.32(17)	1.39
$\mathbf{3^{Ce}}$·Et_2O	172.27(7)	1.40
$\mathbf{3^{U}}$·$THF_{0.8}Et_2O_{0.2}$	172.79(5)	1.40
$\mathbf{3^{Np}}$·Pentane	171.8(3)	1.39
$\mathbf{3^{Pu}}$·$THF_{2/3}Et_2O_{1/3}$	171.29(13)	1.40

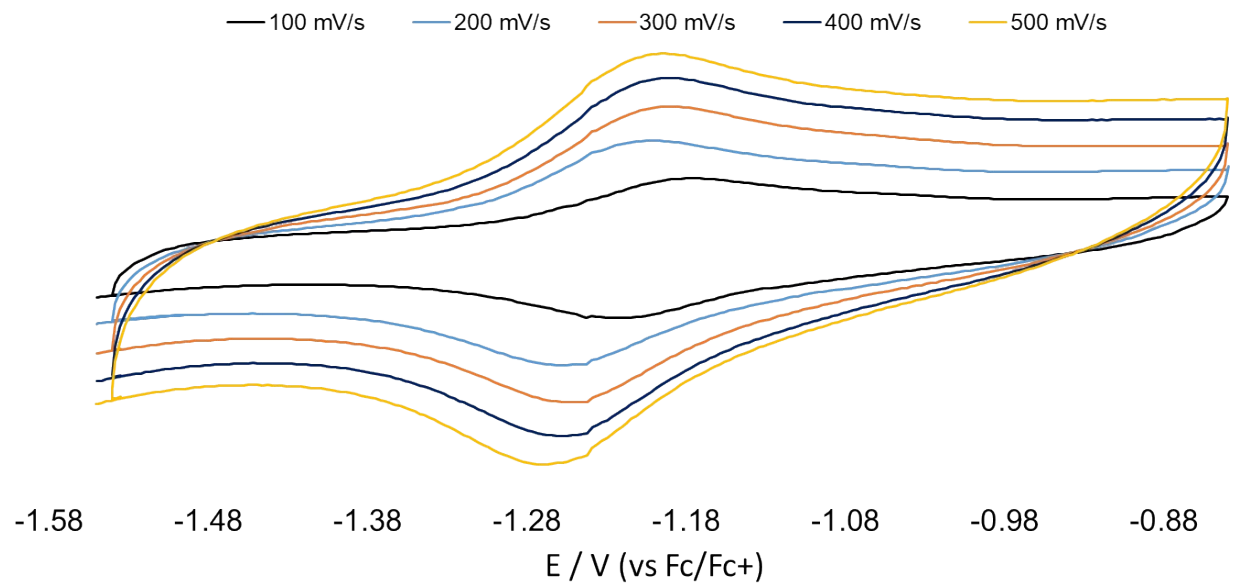

Figure S26. Room temperature cyclic voltammogram of **3**^{Ce} (2.25 mM in THF, 0.26 M [^{n}Pr$_4$N][BArF$_{24}$] supporting electrolyte).

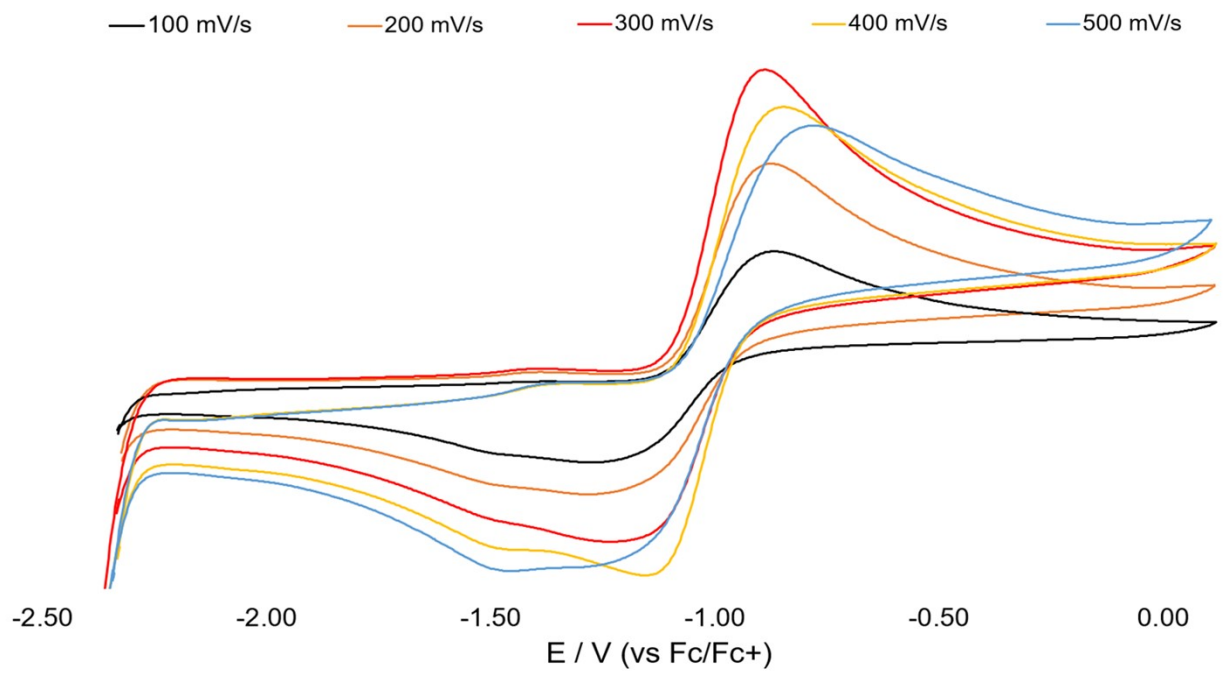

Figure S27. Room temperature cyclic voltammogram of **3**^{U} (2.80 mM in THF, 0.25 M [^{n}Pr$_4$N][BArF$_{24}$] supporting electrolyte).

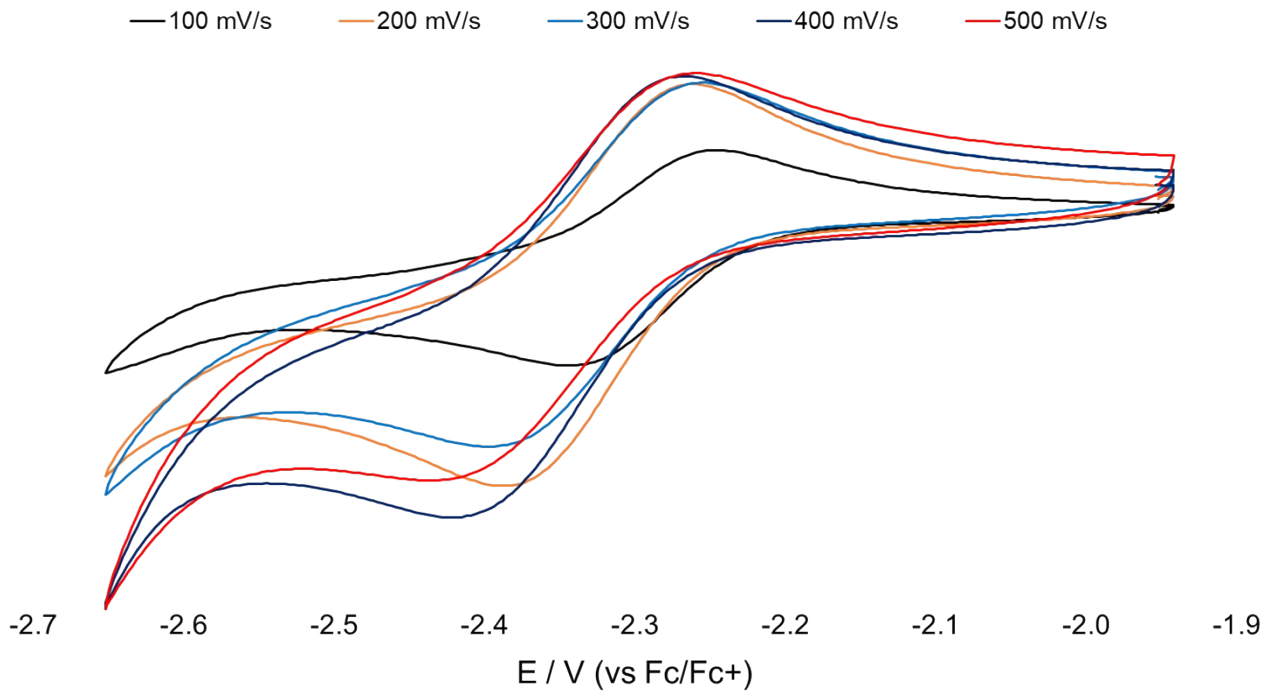

Figure S28. Room temperature cyclic voltammogram of **3^{Np}** (1.89 mM in THF, 0.25 M [^{n}Pr$_4$N][BArF$_{24}$] supporting electrolyte).

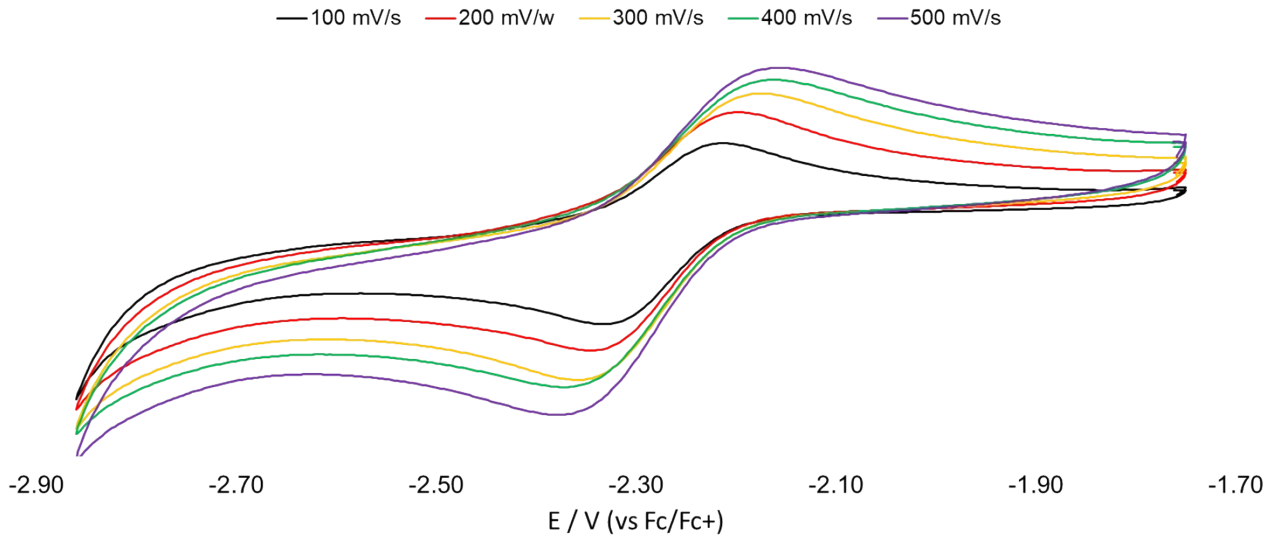

Figure S29. Room temperature cyclic voltammogram of **3^{Pu}** (1.76 mM in THF, 0.21 M [^{n}Pr$_4$N][BArF$_{24}$] supporting electrolyte).

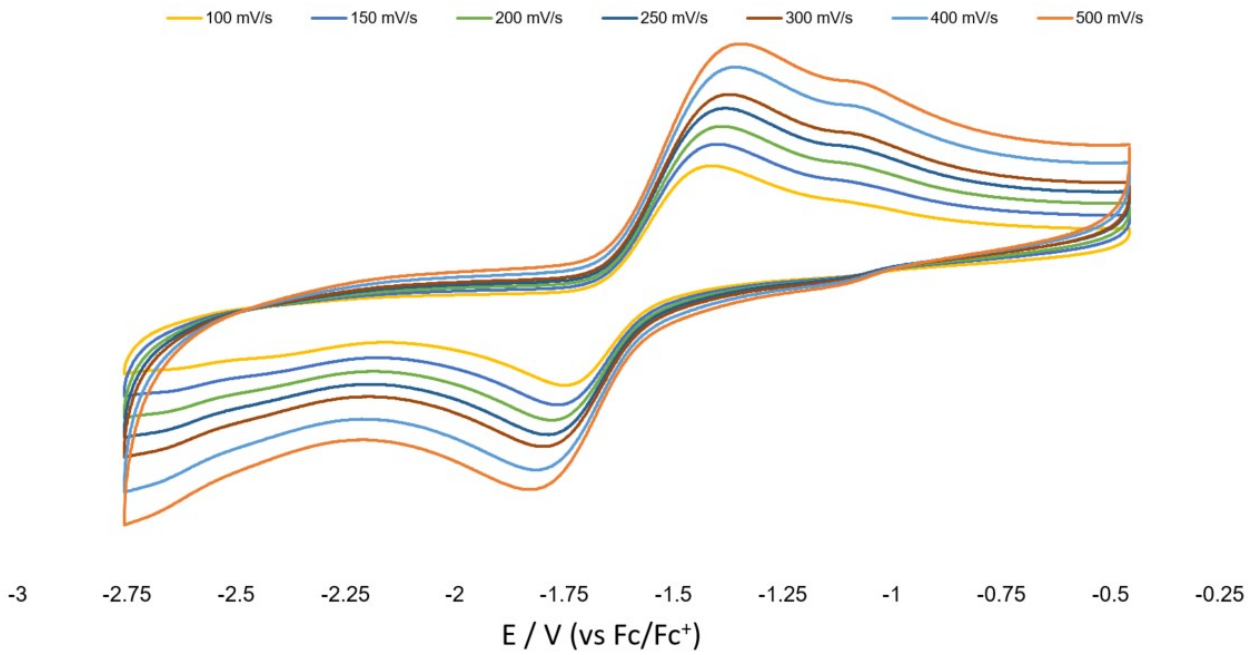

Figure S30. Room temperature cyclic voltammogram of $\mathbf{2^U}$ (4.33 mM in THF**,** 0.10 M $[NBu_4][PF_6]$ supporting electrolyte).

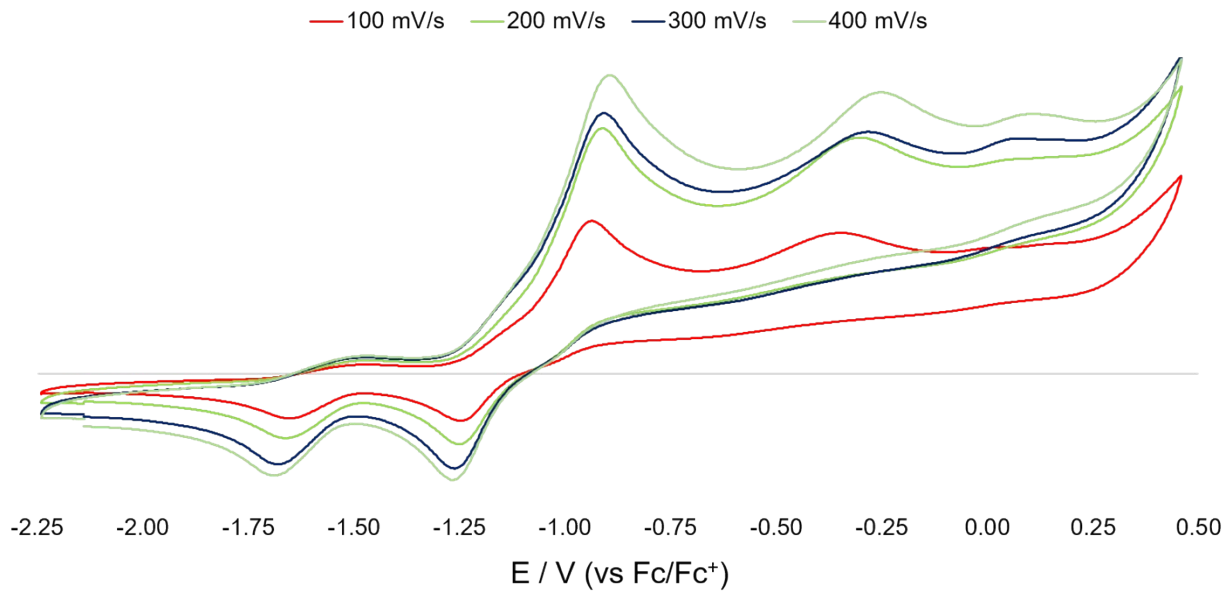

Figure S31. Room temperature cyclic voltammogram of **2**^{Ce} (3.71 mM in THF, 0.25 M [$^{n}Pr_4N$][$BArF_{24}$] supporting electrolyte).

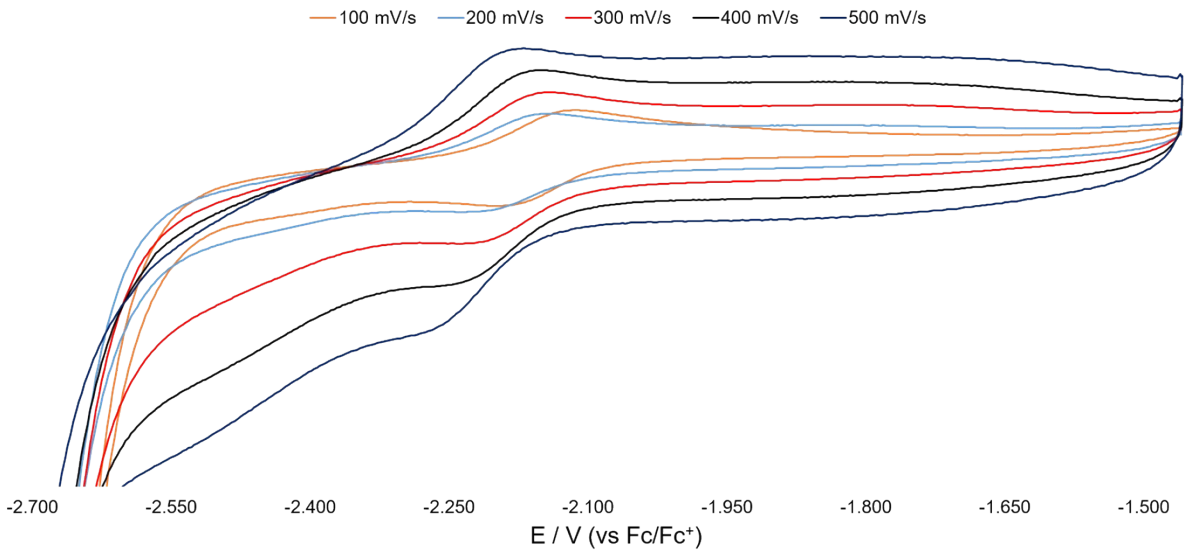

Figure S32. Room temperature cyclic voltammogram of **2^{Np}** (0.93 mM in THF, 0.28 M [^{n}Pr$_4$N][BArF$_{24}$] supporting electrolyte).

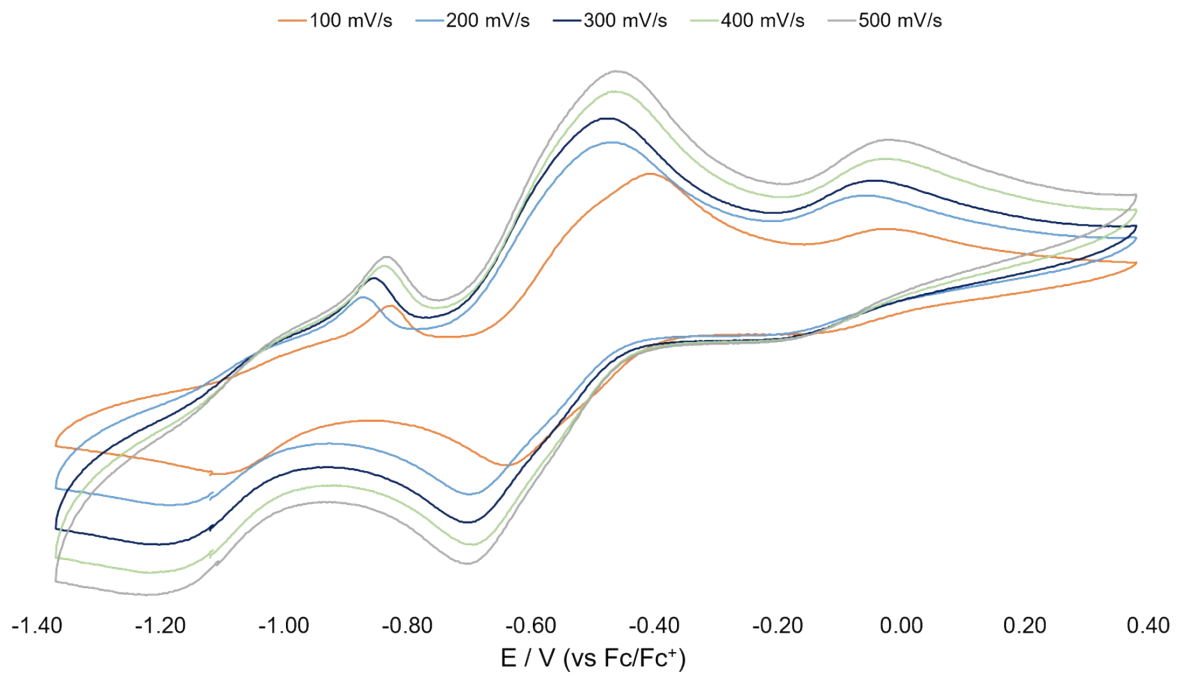

Figure S33. Room temperature cyclic voltammogram of $\mathbf{1^{Np}}$ (3.38 mM in THF, 0.25 M $[^{n}Pr_4N][BArF_{24}]$ supporting electrolyte).

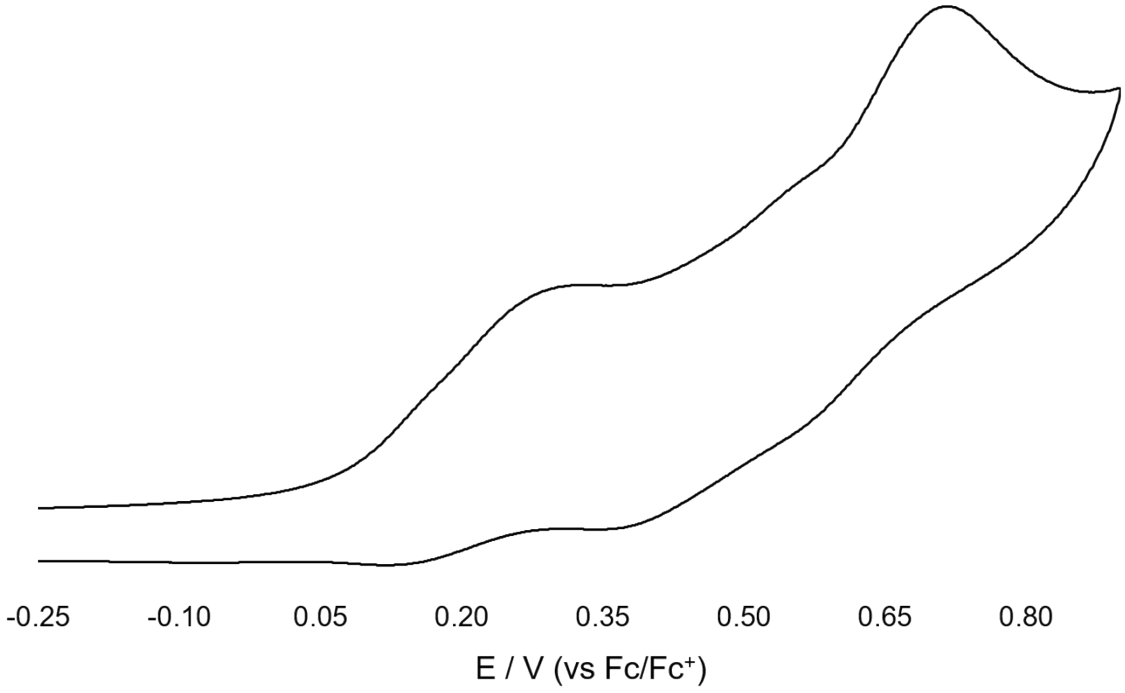

Figure S34. Room temperature cyclic voltammogram of $\mathbf{1}^{Ce}$ (5.55 mM in THF**,** 0.10 M $[NBu_4][PF_6]$ supporting electrolyte).

Complex	E_{pa}(V)	E_{pc}(V)	$E_{1/2}$(V) M(IV)/(III)
$\mathbf{2^{U}}$	-1.76	-1.40	-1.58
$\mathbf{2^{Np}}$	-2.19	-2.11	-2.16
$\mathbf{3^{U}}$	-1.31	-0.83	-1.07
$\mathbf{3^{Np}}$	-2.35	-2.25	-2.30
$\mathbf{3^{Pu}}$	-2.33	-2.21	-2.27

Table S6. Reduction potentials tentatively assigned (see page S61) to M(IV)/(III) couples for selected $\mathbf{2^{M}}$ and $\mathbf{3^{M}}$ complexes taken in THF with [^{n}Pr$_4$N][BArF$_{24}$] supporting electrolyte. Scan rates of 100 mV/s. All data reported vs Fc/Fc^{+} couple. Further investigation is required before more definitive assignments and understanding of the redox events can be reported. We note that if these redox couples are indeed attributable to M(IV)/(III) then they would be appear to be counter-intuitive to the expected trend of increasing stability of the +3 oxidation state across the actinide series.

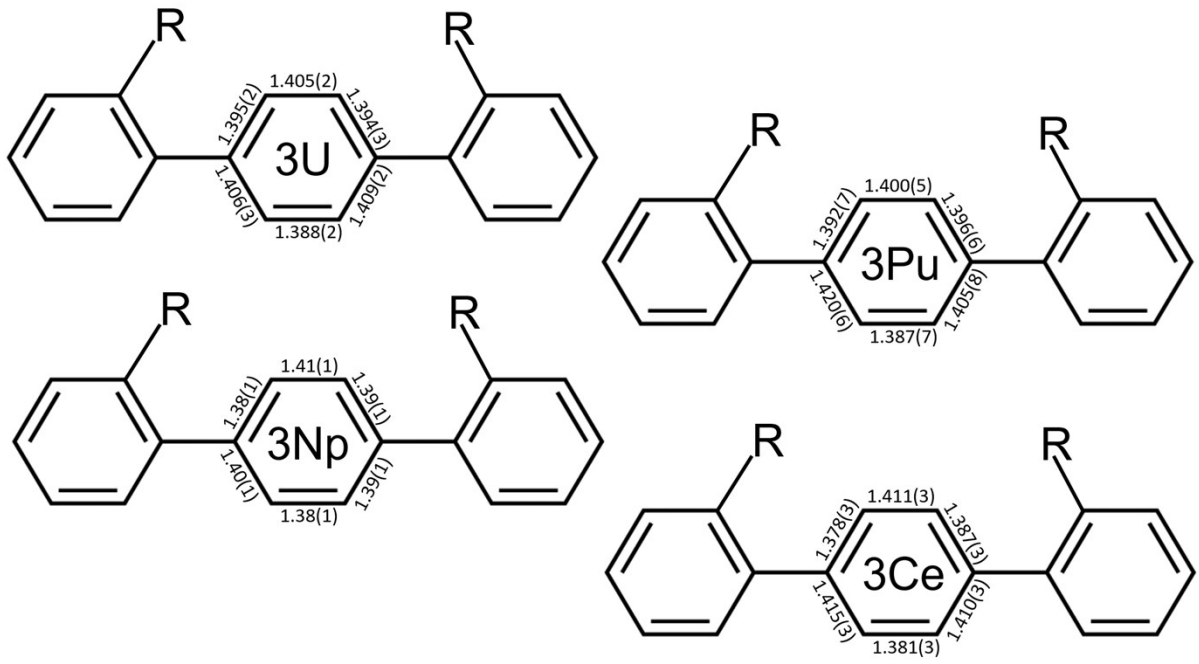

Figure S35. Internal bond distances for the metal η^6-coordinated arene ring in complexes $\mathbf{3^M}$.

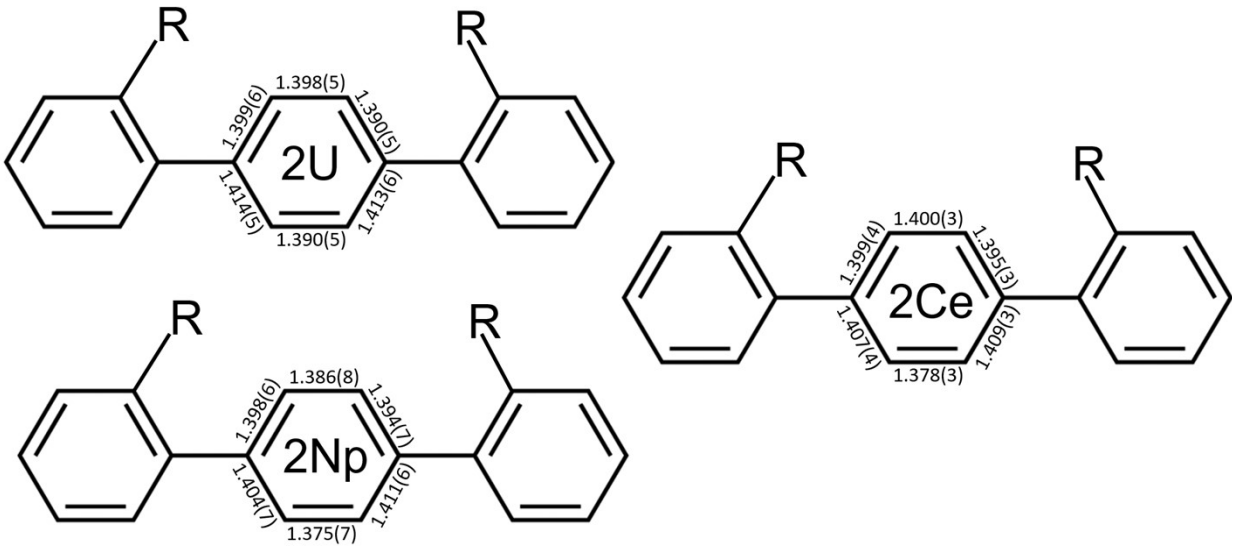

Figure S36. Internal bond distances for the metal η^6-coordinated arene ring in complexes $\mathbf{2^M}$.

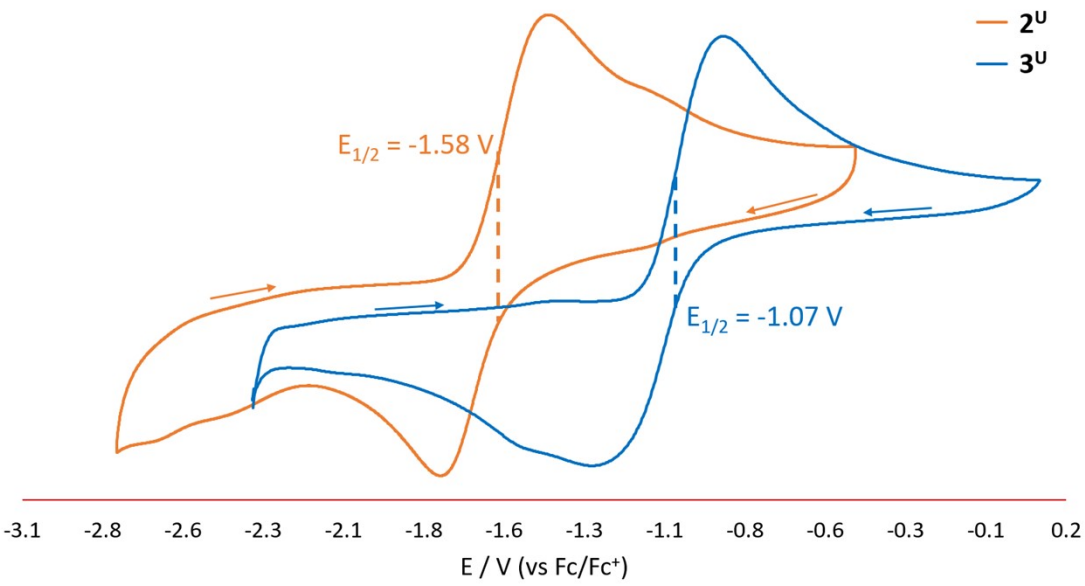

Figure S37. Room temperature cyclic voltammogram of $\mathbf{2^U}$ and $\mathbf{3^U}$ in THF. [^{n}Pr$_4$N][BArF$_{24}$] supporting electrolyte for $\mathbf{3^U}$ and [NBu$_4$][PF$_6$] for $\mathbf{2^U}$. Scan rate of 100 mV/s. Arrows indicate direction of scan.

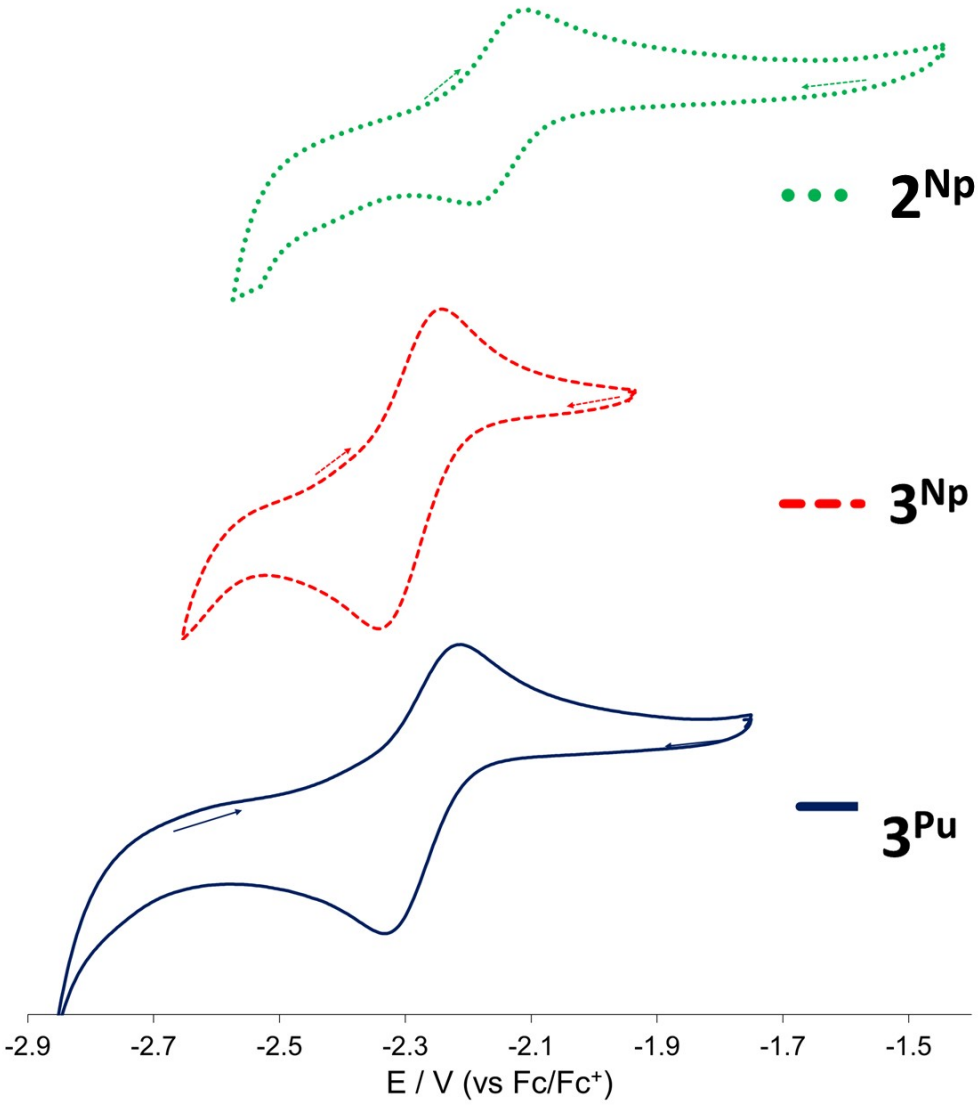

Figure S38. Room temperature cyclic voltammogram of $\mathbf{2^{Np}}$, $\mathbf{3^{Np}}$ and $\mathbf{3^{Pu}}$ in THF and [^{n}Pr$_4$N][BArF$_{24}$] supporting electrolyte. Scan rate of 100 mV/s. Arrows indicate direction of scan.

Electrochemical Studies

In an effort to assess the potentially accessible metal oxidation states of these complexes, we performed cyclic voltammetry (CV) measurements on THF solutions of $\mathbf{1^M}$, $\mathbf{2^M}$ and $\mathbf{3^M}$ complexes. Electrochemical studies of several of the reported complexes resulted in decomposition and unreliable data; however, CV data was successfully measured for $\mathbf{2^{Ce}}$, $\mathbf{2^U}$, $\mathbf{2^{Np}}$, $\mathbf{3^U}$, $\mathbf{3^{Np}}$ and $\mathbf{3^{Pu}}$ (Figures S31, S37 and S38). As is the case with the UV-vis-NIR spectra, the presence of H_2L^{Ar} in solution (as evidenced by NMR spectroscopy) could have some effect upon the cyclic voltammograms. Due to the unexpected complexity of these results and the need for further analysis via complementary voltametric techniques, we plan to incorporate these initial results into a follow-up study.

Complex $\mathbf{2^U}$ presents a redox process centred at a half wave potential ($E_{1/2}$) of -1.58 V (anodic to cathodic peak-to-peak potentials separation (ΔE_p) = 0.36 V) vs Fc/Fc^+ at a scan rate of 100 mV/s (Figure S37). This feature is electrochemically irreversible and remains so at scan rates up to 500 mV/s (Figure S31). This process is attributed to a U(IV/III) redox couple as it falls within close range for other U(IV/III) couples[13] and is comparable to the U(III) complex $Cp_3^{tet}U$ ($Cp^{tet} = C_5Me_4H$), which exhibits an assigned U(IV/III) redox event centred at -1.46 V (vs. Fc/Fc^+).[14] A similar redox feature is observed for $\mathbf{3^U}$, $E_{1/2}$ = -1.07 V (ΔE_p = -0.19 V) vs Fc/Fc^+ at 100 mV/s, which is anodically shifted by 0.51 V as compared to $\mathbf{2^U}$ (Figure S37).

For the neptunium complex $\mathbf{2^{Np}}$, a fully reversible redox event is centred at -2.16 V (ΔE_p = 79 mV) (Figure 6). Moreover, $\mathbf{3^{Np}}$ also contains a fully reversible redox event centred at -2.30 V (vs Fc/Fc^+) at 100 mV/s, with ΔE_p = 49 mV) (Figure S38). Interestingly, the electrochemical analysis of $\mathbf{1^{Np}}$ does not share this reduction feature, but instead displays a

well resolved event at $E_{1/2}$ = 0.55 V (ΔE_p = 0.23 V) (Figure S33). Although there are very few potentiodynamic electrochemical studies on neptunium complexes in a non-aqueous setting, we can compare this redox event to a few relevant examples. In the case of tetravalent $Np^{IV}L'_2$ (H_2L' = *N*,*N*′-bis[(4,4′-diethylamino)salicylidene]-1,2-phenylenediamine), an irreversible redox event at $E_{1/2}$ = -2.91 V (vs Fc/Fc^+) is observed, which was attributed to a Np(IV/III) couple.[15] The tris(amide) neptunium complex $Np(NR_2)_3Cl$ (R = $SiMe_3$) displays a reversible Np(IV/III) couple with $E_{1/2}$ = -1.29 V.[16] While the mono-chloro Np^{4+} complex, [($Tren^{TIPS}$)NpCl] ($Tren^{TIPS}$ = $\{N(CH_2CH_2NSi^iPr_3)_3\}^{3-}$ and ^{i}Pr = isopropyl) possesses a well-defined reversible Np(IV/III) couple at $E_{1/2}$ = -1.85 V (vs Fc/Fc^+).[17]

The cyclic voltammogram of $\mathbf{3^{Pu}}$ is similar to those of $\mathbf{2^{Np}}$ and $\mathbf{3^{Np}}$, with a redox event centred at -2.27 V (vs Fc/Fc^+) with an E_p = 0.12 V at 100 mV/s. Again, comparative data for the plutonium electrochemical analysis, outside of molten salts and aqueous media, is sparse. Electrochemical analysis of $Pu^{IV}[(^t$BuNO)py$]_4$ in THF solutions possessed a Pu(IV/III) couple assigned to a feature centred at -2.53 V (vs Fc/Fc^+), with a computational expectation value of -2.68 V.[18] Given these comparisons, it is reasonable to assign the feature in $\mathbf{3^{Pu}}$ to a Pu(IV/III) couple. A table of reduction potentials for the $\mathbf{2^M}$ and $\mathbf{3^M}$ actinides can be found in Table S6 of the supporting information.

Electrochemical analysis of $\mathbf{2^{Ce}}$ shows two features centred at -1.31 V (E_p = 0.71 V) and -0.78 V (E_p = 0.90 V) (vs Fc/Fc^+), with a third less prominent irreversible feature appearing at 0.11 V at higher scan rates (Figure S31). We attribute the redox event at -1.31 V to the oxidation of Ce^{3+} to Ce^{4+}, which falls in the range of previously reported Ce(IV/III) couples,[19] although the majority of those reports are related to inorganic cerium complexes

in aqueous media. The more closely related cerium complex $[Li(THF)_2Ce(MBP)_2(THF)_2]$ (MBP = 2,2′-methylenebis(6-*tert*-butyl-4-methylphenolate)) exhibits a $E_{1/2}$ = -0.93 V (vs. Fc/Fc^+) in THF, with the large anodic shift contributed to the stabilizing effect of the MBP ligand.[20] The features seen at 0.78 V and 0.11 V we assign to ligand based oxidations.

Electrochemical investigation into $\mathbf{2^M}$ and $\mathbf{3^M}$ redox properties show accessible M(IV/III) oxidation processes, which are reversible in the case of $\mathbf{2^{Np}}$ and $\mathbf{3^{Np}}$, and irreversible complexes $\mathbf{2^U}$, $\mathbf{3^U}$, $\mathbf{3^{Pu}}$ and $\mathbf{2^{Ce}}$. No redox events attributable to a M(III/II) couple were observed within the solvent accessible electrochemical window. Interestingly, the observed events we attribute to III/IV couples appear counter-intuitive to the expected trend as one traverses the actinide series from U to Np to Pu where the +3 oxidation state should become more easily accessible. However, since the observed events cannot be unambiguously assigned at this stage in the investigation then further studies are warranted.

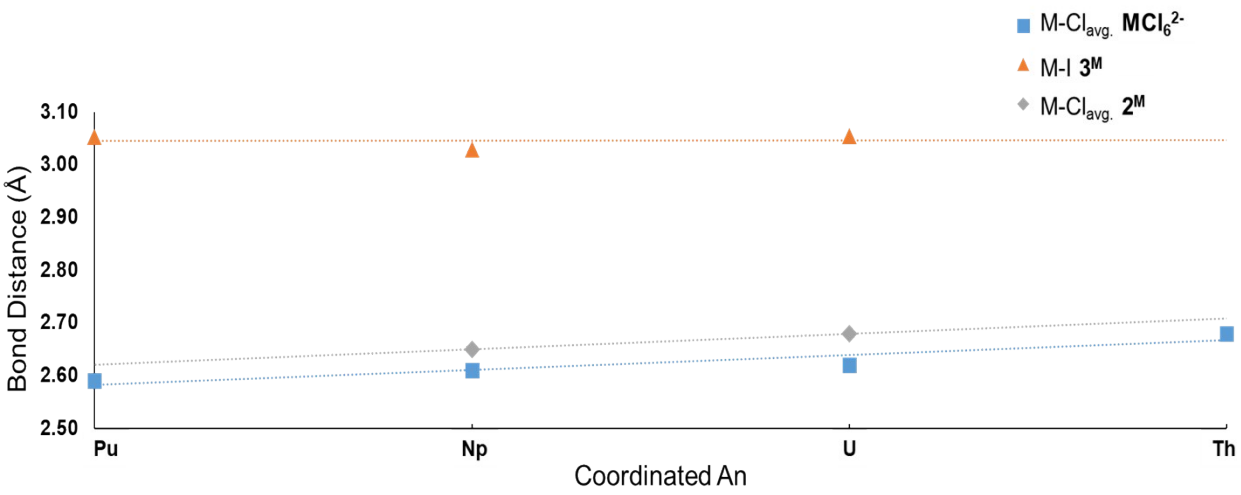

Figure S39. Plot of actinide element identity versus actinide-halide bond distances for $\mathbf{2^M}$, $\mathbf{3^M}$ and $[\mathbf{MCl_6}]^{2-}$ complexes.[21] Dotted lines shown were generated by linear trend line fit.

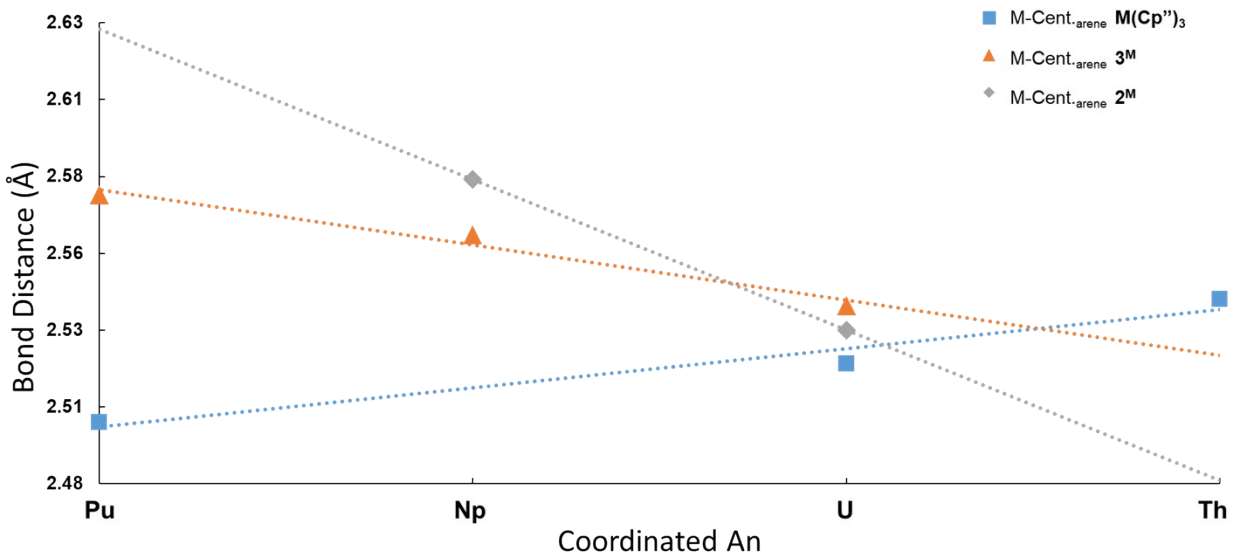

Figure S40. Plot of actinide element identity versus M-arene$_{cent}$ bond distances for **2^{M}**, **3^{M}** and **M(Cp″)$_3$** (where ″ = $C_5H_3(SiMe_3)_2^-$) complexes.[22] Dotted lines shown were generated by linear trend line fit.

References

1. L. R. Avens, S. G. Bott, D. L. Clark, A. P. Sattelberger, J. G. Watkin and B. D. Zwick, *Inorganic Chemistry*, 1994, **33**, 2248-2256.
2. T. V. Fetrow, J. P. Grabow, J. Leddy and S. R. Daly, *Inorganic Chemistry*, 2021, **60**, 7593-7601.
3. C. A. P. Goodwin, M. T. Janicke, B. L. Scott and A. J. Gaunt, *Journal of the American Chemical Society*, 2021, **143**, 20680-20696.
4. S. Fortier, J. R. Aguilar-Calderón, B. Vlaisavljevich, A. J. Metta-Magaña, A. G. Goos and C. E. Botez, *Organometallics*, 2017, **36**, 4591-4599.
5. Scott, B. L. Actinide Research Quarterly; LA-UR-15-24862; Los Alamos National Laboratory: 2015; pp 6-9. DOI: https://doi.org/10.2172/1188164
6. SMART Apex II,Version 2.1; Bruker AXS Inc.: Madison, WI
7. SAINT Software User's Guide,Version 7.34a; Bruker AXS Inc.: Madison, WI
8. Blessing, R.Acta Crystallogr. A1995, A51
9. Sheldrick, G. M. SHELXTL,6.12; Bruker Analytical X-Ray Systems, Inc.: Madison, WI
10. Dolomanov, O. V.; Bourhis, L. J.; Gildea, R. J.; Howard, J. A. K.; Puschmann, H. J. Appl. Cryst.2009, 42, 339
11. J.-S. Jiang and A. T. Brünger, *Journal of Molecular Biology*, 1994, **243**, 100-115.
12. P. Van Der Sluis and A. L. Spek, *Acta Crystallographica Section A*, 1990, **46**, 194-201.
13. L. R. Avens, D. M. Barnhart, C. J. Burns, S. D. McKee and W. H. Smith, *Inorg Chem*, 1994, **33**, 4245-4254.
14. J. C. Wedal, J. M. Barlow, J. W. Ziller, J. Y. Yang and W. J. Evans, *Chem Sci*, 2021, **12**, 8501-8511.
15. B. E. Klamm, C. J. Windorff, C. Celis-Barros, M. J. Beltran-Leiva, J. M. Sperling and T. E. Albrecht-Schönzart, *Inorganic Chemistry*, 2020, **59**, 18035-18047.
16. S. L. Staun, L. M. Stevens, D. E. Smiles, C. A. P. Goodwin, B. S. Billow, B. L. Scott, G. Wu, A. M. Tondreau, A. J. Gaunt and T. W. Hayton, *Inorganic Chemistry*, 2021, **60**, 2740-2748.
17. M. S. Dutkiewicz, C. A. P. Goodwin, M. Perfetti, A. J. Gaunt, J.-C. Griveau, E. Colineau, A. Kovács, A. J. Wooles, R. Caciuffo, O. Walter and S. T. Liddle, *Nature Chemistry*, 2022, **14**, 342-349.
18. J. Su, T. Cheisson, A. McSkimming, C. A. P. Goodwin, Ida M. DiMucci, T. Albrecht-Schönzart, B. L. Scott, E. R. Batista, A. J. Gaunt, S. A. Kozimor, P. Yang and E. J. Schelter, *Chemical Science*, 2021, **12**, 13343-13359.
19. J. R. Levin, W. L. Dorfner, A. X. Dai, P. J. Carroll and E. J. Schelter, *Inorganic Chemistry*, 2016, **55**, 12651-12659.
20. B. D. Mahoney, N. A. Piro, P. J. Carroll and E. J. Schelter, *Inorganic Chemistry*, 2013, **52**, 5970-5977.
21. S. G. Minasian, K. S. Boland, R. K. Feller, A. J. Gaunt, S. A. Kozimor, I. May, S. D. Reilly, B. L. Scott and D. K. Shuh, *Inorganic Chemistry*, 2012, **51**, 5728-5736.
22. O. Walter, *Chemistry – A European Journal*, 2019, **25**, 2927-2934.